Monthly Notices of the ROYAL ASTRONOMICAL SOCIETY
MNRAS **520,** 4562–4581 (2023) https://doi.org/10.1093/mnras/stad135

The Thousand-Pulsar-Array programme on MeerKAT – VIII. The subpulse modulation of 1198 pulsars

X. Song [1]★ P. Weltevrede [1] A. Szary [2,3] G. Wright,[1] M. J. Keith,[1] A. Basu [1] S. Johnston [4] A. Karastergiou,[5] R. A. Main [6] L. S. Oswald [5,7] A. Parthasarathy [6] B. Posselt [5,8] M. Bailes,[9,10] S. Buchner [11] B. Hugo[11,12] and M. Serylak [13,14]

[1]*Jodrell Bank Centre for Astrophysics, Department of Physics and Astronomy, University of Manchester, Manchester M13 9PL, UK*
[2]*Janusz Gil Institute of Astronomy, University of Zielona Góra, Licealna 9, PL-65-417 Zielona Góra, Poland*
[3]*ASTRON, Netherlands Institute for Radio Astronomy, Oude Hoogeveensedijk 4, NL-7991 PD Dwingeloo, the Netherlands*
[4]*Australia Telescope National Facility, CSIRO Space and Astronomy, PO Box 76, Epping, NSW 1710, Australia*
[5]*Department of Astrophysics, University of Oxford, Denys Wilkinson Building, Keble Road, Oxford OX1 3RH, UK*
[6]*Max-Plank-Institut für Radioastronomie, Auf dem Hügel 69, D-53121 Bonn, Germany*
[7]*Magdalen College, University of Oxford, Oxford OX1 4AU, UK*
[8]*Department of Astronomy & Astrophysics, Pennsylvania State University, 525 Davey Lab, University Park, PA 16802, USA*
[9]*Centre for Astrophysics and Supercomputing, Swinburne University of Technology, PO Box 218, Hawthorn, VIC 3122, Australia*
[10]*ARC Centre of Excellence for Gravitational Wave Discovery (OzGrav) , Swinburne University of Technology, PO Box 218, Hawthorn, VIC 3122, Australia*
[11]*South African Radio Astronomy Observatory (SARAO), 2 Fir Street, Black River Park Observatory, Cape Town 7925, South Africa*
[12]*Department of Physics and Electronics, Rhodes University, Artillery Road, Grahamstown 6139, South Africa*
[13]*SKA Observatory, Jodrell Bank, Lower Withington, Macclesfield SK11 9FT, UK*
[14]*Department of Physics and Astronomy, University of the Western Cape, Bellville, Cape Town 7535, South Africa*

Accepted 2023 January 13. Received 2022 December 21; in original form 2022 July 25

ABSTRACT

We report on the subpulse modulation properties of 1198 pulsars using the Thousand-Pulsar-Array programme on MeerKAT. About 35 per cent of the analysed pulsars exhibit drifting subpulses that are more pronounced towards the death line, consistent with previous studies. We estimate that this common phenomenon is detectable in 60 per cent of the overall pulsar population if high-quality data were available for all. This large study reveals the evolution of drifting subpulses across the pulsar population in unprecedented detail. In particular, we find that the modulation period P_3 follows a V-shaped evolution with respect to the characteristic age τ_c, such that the smallest P_3 values, corresponding to the Nyquist period $P_3 \simeq 2$, are found at $\tau_c \simeq 10^{7.5}$ yr. The V-shaped evolution can be interpreted and reproduced if young pulsars possess aliased fast intrinsic P_3, which monotonically increase, ultimately achieving a slow unaliased P_3. Enhancement of irregularities in intrinsic subpulse modulation by aliasing in small-τ_c pulsars would explain their observed less well defined P_3's and weaker spectral features. Modelling these results as rotating subbeams, their circulation must slow down as the pulsar evolves. This is the opposite to that expected if circulation is driven by $\boldsymbol{E} \times \boldsymbol{B}$ drift. This can be resolved if the observed P_3 periodicity is due to a beat between an $\boldsymbol{E} \times \boldsymbol{B}$ system and the pulsar period. As a by-product, we identified the correct periods and spin-down rates for 12 pulsars, for which harmonically related values were reported in the literature.

Key words: catalogues – pulsars: general.

1 INTRODUCTION

Radio signals from pulsars have been observed for over five decades, with the highly magnetized and compact nature of pulsars making them unique laboratories to study physics under extreme conditions. The pulses from single stellar rotations have shown much larger variations in intensity and pulse phase compared to the average pulse shape, and often show subpulses with much narrower pulse widths. These single pulses always show a degree of apparent random pulse-to-pulse variability, but this is often accompanied by a high degree of organization. In many pulsars, subpulses 'march' through the pulse profile window (Drake & Craft 1968), now more commonly known as 'drifting' subpulses. The single pulses form diagonal 'drift bands' in the pulse stack (see e.g. fig. 1 in Weltevrede, Edwards & Stappers 2006 and online material D1), and the drift patterns can be quantified via P_3 and P_2 as the repeat separation between drift bands (in the pulse number direction expressed in a number of rotational periods P) and between successive subpulses (in the pulse phase direction), respectively. Unlike P_3, P_2 depends on observing frequency and pulse longitude. It is therefore in general different in different profile components (e.g. Weltevrede et al. 2006; Weltevrede, Stappers & Edwards 2007). This makes P_2 a somewhat ill-defined quantity.

★ E-mail: xsong@pulsarastronomy.net

Subpulse drift has been found to be a complex phenomenon. For example, the observed P_3 and P_2 values can be complicated by the effect of aliasing, which occurs if the intrinsic periodicity of the observed pattern (P_3) is less than twice our sampling rate ($P_3 < 2$). This results in the observed P_3 being larger than its intrinsic value (e.g. PSR B0943+10 by Deshpande & Rankin 1999; Gil & Sendyk 2003). The P_2 values can be different for different pulse profile components. In some cases, the drift bands are such that the subpulses are stationary in phase, and only amplitude modulations are seen (e.g. Weltevrede et al. 2006; Basu et al. 2016). In others, the subpulses associated with different pulse profile components are observed to drift in opposite directions at a given time (so-called bi-drifting pulsars; see e.g. Qiao et al. 2004; Champion et al. 2005; Weltevrede 2016; Szary & van Leeuwen 2017; Wright & Weltevrede 2017). The drifting subpulse pattern has also been found to occasionally switch among different forms, referred to as drift mode changes (e.g. Huguenin, Taylor & Troland 1970). In these cases, their drift rates typically have a consistent P_2 but different P_3 values. In contrast, other pulsars continuously change their apparent drift direction as a function of time (e.g. PSRs B0826−34, Biggs et al. 1985; Gupta et al. 2004; B0540+23, Nowakowski 1991; J1750−3503, Szary et al. 2022).

More dramatic forms of mode changing can also occur, with one mode exhibiting drifting subpulses and the other having disorganized subpulse modulation (e.g. PSR B0943+10; Deshpande & Rankin 2001). Both kinds of mode change can result in average pulse profiles switching between different stable shapes over long time-scales. A further not uncommon phenomenon is 'nulling', which is observed when emission ceases for a few pulses to hundreds of pulse periods (e.g. Taylor & Huguenin 1971; Wang, Manchester & Johnston 2007), and can be thought of as an extreme case of mode changing. The mode changing phenomenon, as well as nulling (the data presented here will be analysed for nulling in Keith et al., in preparation), adds variability with a characteristic time-scale to the observed emission, which can complicate the detection of periodicities associated with drifting subpulses.

In addition to studying the single pulse phenomena of individual sources, large surveys of subpulse modulation help identify trends in the pulsar population and constrain the underlying emission processes. A single observational set-up, fixed frequency band, and systematic approach in the analysis provide additional benefits. Early surveys of subpulse modulation include Backus (1981) and Ashworth (1982), where 20 and 52 sources were assessed at around 400 MHz and they found about half of the sample showing drifting subpulses. Rankin (1986) collected statistics of pulsars with drifting subpulses and empirically linked this phenomenon to the pulse profile morphology. Single pulse observations dedicated to the systematic study of such pulsars were carried out centred at a wavelength of ∼21 and ∼92 cm by Weltevrede et al. (2006, 2007) using the Westerbork Synthesis Radio Telescope (WSRT). In particular, by analysing 187 pulsars, the 21 cm survey significantly increased the number of pulsars with known drifting subpulses by discovering this phenomenon in 42 pulsars. This unbiased search for pulsar subpulse modulation concluded, after taking the signal-to-noise ratio (S/N) of the data into account, that more than 50 per cent of pulsars exhibit drifting subpulses or periodic modulation features. It therefore represents a very common phenomenon throughout the pulsar population. In addition, these results confirmed the finding of Wolszczan (1980), Ashworth (1982), and Rankin (1986) that pulsars of large characteristic age are more likely to have detectable drifting subpulses with more precise drift features.

Basu et al. (2016, 2019) studied 123 pulsars using the Giant Metrewave Radio Telescope (GMRT) at low frequency (at 618 and 333 MHz), of which 61 show drifting subpulses. They found an anticorrelation between P_3 and the spin-down energy loss rate $\dot{E}$, with typically larger P_3 values present at low $\dot{E}$. In particular, pulsars with conal profile components, usually with $\dot{E} < 5 \times 10^{32}$ erg s^{-1}, are more likely to have drifting subpulses (see also Rankin 1986). Pulsars with $\dot{E}$ above this boundary have core-dominated pulse profiles and amplitude modulation (without detectable drift) with large P_3.

Theoretical explanations of drifting subpulses were established relatively early after their discovery. The most well developed model is the well-known Ruderman & Sutherland (1975) model. These authors attribute drifting subpulses to a rotating 'carousel' of discrete sparks (discharges) that are formed in a gap (charge depleted region) above the neutron star surface. The electron–positron pairs produced in the discharges are responsible for the observed radio emission. A circulation of the carousel of radio beamlets around the magnetic axis, due to the $\boldsymbol{E} \times \boldsymbol{B}$ drift, is predicted. The circulation time-scale of the carousel together with the number of sparks defines the P_3 of the observed pattern of drifting subpulses. Varying drift rates can then be thought of as changes in the number of beamlets or rotation speed of the carousel.

The sparking gap model was further developed by e.g. Gil, Melikidze & Geppert (2003) allowing for an additional screening of the electric field in the vacuum gap. In contrast to the classical picture, Basu et al. (2016) discussed the possibility that for a pulsar with a magnetic dipole axis inclined to the rotation axis, the sparks circulate around the rotation axis rather than the magnetic axis. Very different geometrical interpretations of drifting subpulses have been proposed. For example, Rosen & Clemens (2008) proposed a non-radial oscillation model without invoking circulations in the magnetosphere. Gogoberidze et al. (2005) suggested that drifting subpulses are due to modulation in the emission region generated by drift waves, in some form of magnetospheric oscillations.

Here, we aim to establish evolutionary trends of drifting subpulses, and subpulse modulation in general. This requires great sensitivity and sufficiently long pulse sequences. The MeerKAT Thousand-Pulsar-Array (TPA) project is designed to observe over a thousand Southern hemisphere pulsars, a large fraction of the total known pulsar population, with a uniform observing set-up. This provides an unprecedented view on the pulsar population. The MeerKAT telescope consists of 64 dishes, with an effective diameter of around 13 m each. The full array has a total system equivalent flux density of 7.5 mJy, a receiver temperature of 18 K, and a wide bandwidth of around 642 MHz at the *L*- band for single pulse studies (Johnston et al. 2020). The adopted observing strategy resulted in at least one long observation with high instantaneous sensitivity, as well as regular observations utilizing subarrays (see Song et al. 2021, for a detailed description of the TPA legacy data sets).

We report on the findings of a systematic analysis of subpulse modulations for 1198 pulsars in the TPA legacy data. This is the largest subpulse modulation survey to date, with in total 1.6 million stellar rotations being analysed. A catalogue of subpulse modulation properties for a significant fraction of the known pulsars is provided, and various trends across the pulsar population are identified.

The structure of the paper is as follows: Section 2 describes how drifting subpulses are identified in the spectral domain. The used sample is defined in Section 3, and the results from the identification of drifting subpulses are compared with results from other major drifting subpulse surveys. In Section 4, the fraction of pulsars with periodic subpulse modulation in the pulsar population is quantified, and

correlations with P and $\dot{P}$ (spin-down rate) are identified in Section 5. Implications of our findings are discussed in Section 6, followed by conclusions. Online materials[1] include a table summarizing all our measured subpulse modulation properties, and figures presenting the fluctuation spectra for all sources in the analysed sample, as well as additional descriptions related to the adopted data analysis pipeline and complementary statistical analysis.

2 OBSERVATIONS AND DATA PROCESSING

2.1 Recording and generation of single-pulse data

The data were observed with the *L*-band receivers (with a centre frequency that is precisely 1283.582 031 25 MHz) of the MeerKAT array, and recorded by the PTUSE[2] instrument in single-pulse observing mode (Bailes et al. 2020). This produced filterbank data with a channel width of 0.835 9375 MHz and ∼38.28 μs time resolution. The recorded bandwidth is 642 MHz for data recorded between 2019 May and 2020 February 10, and 856 MHz otherwise.

After recording, the data are further processed using the methodology in Keith et al. (in preparation). In this process, the filterbank data from the telescope are 'folded' using DSPSR (van Straten & Bailes 2011), producing an archive containing a sequence of pulses for each pulse period. Where possible, it is ensured that the boundaries between different pulse numbers do not coincide with observable emission. Polarization calibration is applied, and the most by radio frequency interference (RFI) affected frequency channels are removed. A set of fully frequency-averaged single-pulse archives is produced for each observation. The science ready data are analysed for subpulse modulation, which is described next.

2.2 Profile alignment and on-pulse identification

A PYTHON script generates and executes a sequence of shell commands that perform spectral analysis in an automated way using PSRSALSA[3] (see Section 2.3) and extract statistical information from the generated output.

The process starts by combining the single-pulse data for a given observation as produced by the process described in Section 2.1 to form a continuous pulse stack suitable for further processing. The data are aligned with a smooth representation of the pulse profile that we will refer to as the 'template' (see Posselt et al. 2021, for details about how these are generated). These steps are performed using PSRCHIVE tools (Hotan, van Straten & Manchester 2004).

Before spectral analysis can take place, the pulse phase ranges corresponding to the on-pulse and off-pulse (no detectable signal from the pulsar) regions need to be identified. This is determined automatically where possible, but is defined manually where needed.

The algorithm identifies a main pulse (MP) and possibly an additional interpulse (IP) interval based on the template. As described in Section 2.3.3, some of the further analysis benefits from splitting the on-pulse regions. Up to two pulse longitude intervals of interest can be specified, which we will refer to as 'components'. As an example, columns (a) and (b) in Fig. 1 correspond to pulsars without an IP detected (no MP/IP next to the pulsar name), while the other pulsars have an IP (the corresponding IP figures can be found in the online material). Panel (a i) of Fig. 1 shows the pulse profile of PSR J1539−6332 (solid line). This double-peaked profile has been split into two components, indicated by the different shaded regions underneath the profile. In contrast, the profile of PSR J1539−4828 (panel b i) is treated as a single component.

Appendix B has further information related to the definition of on- and off-pulse regions. The off-pulse regions are required for baseline subtraction (see Section 2.3.1) and analysis of the spectra (see Sections 2.3.2 and 2.3.3). For seven pulsars, the profile is too wide so that no suitable regions can be identified for off-pulse subtraction, which affects some of the further processing (see Section 2.3). These are excluded from the analysis where relevant as explained in Section 5.

2.3 Spectral analysis

All further processing is done using PSRSALSA, and we refer to Weltevrede (2016) and references therein for additional descriptions of the techniques used. The procedure is summarized below, with an emphasis on extensions to the methodology developed for this survey.

2.3.1 Baseline subtraction and RFI rejection

By default the 'baseline' is subtracted for each individual pulse by fitting a first-order polynomial to the off-pulse regions. This deals with slow (compared to P) variations in the baseline. This option is set for most pulsars, except for seven pulsars (see online material D2) with small off-pulse regions, where the slope subtraction would otherwise introduce variability in the baseline.

The process described in Section 2.1 identifies, and removes, the frequency channels worst affected by RFI. See online material D3 for details of further RFI rejection, with typically a modest 3 per cent of analysed pulses affected.

2.3.2 LRFS and modulation index

The longitude-resolved fluctuation spectrum (LRFS; Backer 1970) is computed by calculating the fast Fourier transform (FFT) of sequences of flux densities for successive pulse longitudes. The LRFS helps to identify periodic emission and reveals the pulse longitudes for which the periodicity occurs. It can also be used to compute the longitude-resolved modulation index, which is a measure of variability defined as the standard deviation of the signal divided by the mean. An advantage of calculating it via the spectral domain is that the off-pulse spectral response is subtracted from the LRFS (reducing the power in the power spectrum). As a consequence, the bias on the modulation index introduced by the white noise and possible remaining variations in the baseline is suppressed. Periodic RFI, affecting a narrow range of fluctuation frequencies, can be effectively excluded from the analysis in the spectral domain. This has been done for 17 pulsars (see online material D3).

The optimum pulse longitude resolution is determined automatically by considering the fraction of pulse longitude bins for which a significant modulation index could be detected (see online material D4). The FFT length is automatically determined by considering the number of spectral bins in the LRFS with a significant detection of spectral power for most pulsars (see Appendix B for details).

In the figures, the dynamic range in the spectra is optimized to emphasize the weaker spectral features (see Appendix B for details). An example LRFS is shown as a grey-scale map in panel (a ii)

[1] Available on zenodo via 10.5281/zenodo.6900582.
[2] Pulsar Timing User Supplied Equipment.
[3] https://github.com/weltevrede/psrsalsa

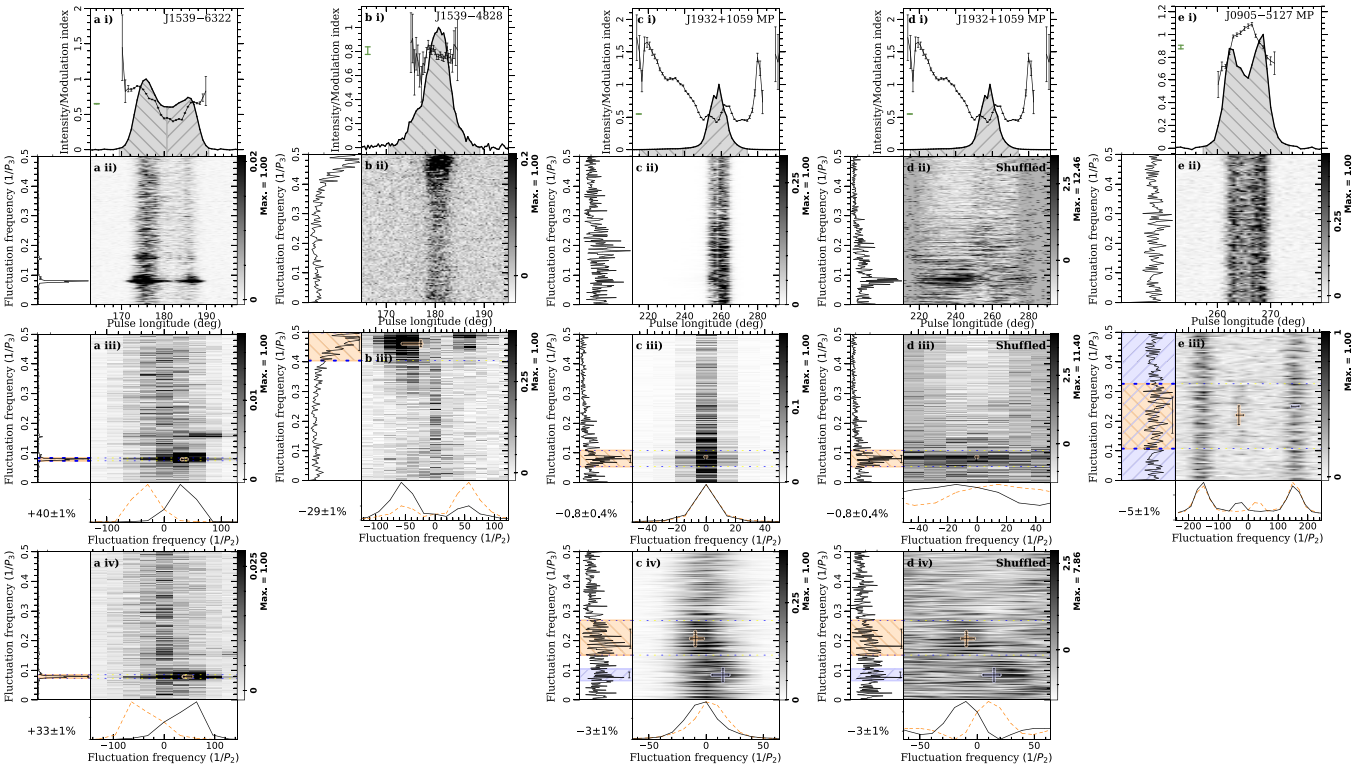

Figure 1. *Column (a)*: a sharp spectral drifting subpulse feature and its harmonic. *Column (b)*: a spectral feature near the $P_3 = 2$ alias border. *Column (c)*: the spectral results of PSR J1932+1059. *Column (d)*: the shuffle-normalized spectra for the same pulsar as column (c). A $1/P_3 \simeq 0.08$ cpp spectral feature dominates the appearance of the shuffle-normalized LRFS at a pulse longitude range between 220° and 250°, which is invisible in column (c). Similarly, the spectral features corresponding to drifting subpulses are also much clearer in the shuffle-normalized 2DFS in panels (d iii) and (d iv). *Column (e)*: a P_2-only spectral feature (vertical bands of power extending the full $1/P_3$ range in panel e iii), as well as a weaker feature associated with drifting subpulses as indicated with a cross in the 2DFS. *Panels (i)* show the normalized average pulse profile (solid line) and modulation indices (points with error bars, with $\bar{m}$ shown at the far left). The LRFS *(panels ii)* cover the same pulse longitude range. For each pulsar, there is at least one (*panels iii*), and sometimes a second (*panels iv*) 2DFS, corresponding to the shaded hatched regions under the pulse profile. All spectra have a colour bar corresponding to spectral power, which can have a maximum value less than that indicated as 'Max.' next to it. If so, the brighter features are clipped such that samples exceeding this threshold value are set to the darkest colour, thereby putting more emphasis to weaker features. The horizontally integrated power in all spectra is shown in the left side panels. The power in the 2DFS is vertically integrated between the dotted lines, or the full range when no dotted lines are shown in the 2DFS. This is shown in the bottom panels (solid line) attached to the 2DFS. The dashed line is mirrored about $1/P_2 = 0$ to highlight asymmetries. For each spectral feature with a P_2 and P_3 measurement, their values are shown as small black error bars on the 2DFS and the shaded region in the left side panels indicates the spectral range included in the measurement. When multiple spectral features are analysed in the same 2DFS, different colours are used. The error bars in the left side panels correspond to σ_{1/P_3} (not visible for PSR J1539−6322) and the dotted lines highlight for each 2DFS the dominant spectral feature with a P_3 value measured. The thicker dotted lines indicate the dominant feature of the pulsar. The percentage indicated for each 2DFS corresponds to $P_{\rm asym}$. See Section 2.3 for more details.

of Fig. 1 for PSR J1539−6322.[4] The horizontal axis of the LRFS corresponds to the pulse longitude in degrees, which is aligned with the pulse profile shown above. The vertical axis corresponds to the $1/P_3$ fluctuation frequency in cycles per period (cpp), where P_3 is the vertical separation between drift bands. The horizontally integrated power is shown in the side panel. The LRFS for PSR J1539−6322 shows a sharp spectral feature seen across the pulse at $1/P_3 \simeq 0.08$ cpp, corresponding to $P_3 \simeq 12$. Weaker spectral features (lighter colours) are seen at other fluctuation frequencies. Some are associated with stochastic subpulse modulation, although in this case the $1/P_3 \simeq 0.16$ cpp feature is the first harmonic of the fundamental frequency. No drifting subpulses were reported before for this pulsar.

Weltevrede et al. (2006, 2007) analysed the minimum in the longitude-resolved modulation index. An alternative way to extract a single value for the modulation index is to compute it weighted by the flux density and averaged over pulse longitude (for both the MP and IP), which we define as

$$\bar{m} = \frac{\sum_i m_i I_i}{\sum_i I_i} = \frac{\sum_i \sigma_i}{\sum_i I_i}. \quad (1)$$

Here, for on-pulse bin i the longitude-resolved modulation index and standard deviation[5] are m_i and σ_i, respectively, and I_i is the flux density of the profile. In the last step in equation (1), we used the definition $m_i \equiv \sigma_i/I_i$. The errors on m_i and $\bar{m}$ are derived using bootstrapping (see Weltevrede 2016). In equation (1), m_i for all on-pulse pulse longitude bins are included, regardless of their significance. The longitude-resolved modulation indices are shown as solid points with error bars in panels (i) in Fig. 1, and that of $\bar{m}$ is indicated at the far left in the same panels.

[4]Single pulses of this pulsar are shown in the online material D1.

[5]Since the off-pulse spectrum has been subtracted from the LRFS, the spectral power-derived variance σ_i^2 can be negative. In those cases, σ_i is taken to be $-(-\sigma_i^2)^{1/2}$.

Weltevrede et al. (2006) suggested the use of the minimum in the longitude-resolved modulation index, because the modulation index tends to be the largest where the pulse profile is weak. So the minimum should be relatively free from an S/N bias. In this work, we prefer the use of $\bar{m}$, as it incorporates the emission from all pulse longitudes for which emission is detected.

To check the S/N bias, simulations have been done by adding white noise to pulsar data. This shows that there is still an S/N bias in the minimum m_i arising from the fact that a smaller m_i requires a higher S/N to become significant. The simulations show that $\bar{m}$ is less susceptible to such a bias. However, there is a bias for S/N $\lesssim$ 100 such that the measured $\bar{m}$ tends to be too low. The analysis in Section 5.6 takes this into account.

2.3.3 2DFS evaluation

The LRFS, when computed as a power spectrum (Section 2.3.2) and as shown in for example Fig. 1, does not reveal whether periodic subpulse modulation corresponds to subpulse drifting (phase modulation) or longitude stationary (amplitude) modulation. Phase drift can be revealed using the two-dimensional fluctuation spectrum (2DFS). The 2DFS is the power spectrum obtained by computing FFTs in both the pulse longitude and the pulse number direction (Edwards & Stappers 2002). The used pulse longitude resolution and the FFT sizes are the same as those used to compute the LRFS. The FFTs in the pulse longitude direction are restricted to the profile components (indicated by the shaded regions of the pulse profiles in panels i) of Fig. 1), and up to two 2DFSs are calculated per MP and IP. As for the LRFSs, the dynamic range is adjusted to ensure weak features are visible (see Appendix B) and an off-pulse spectrum is subtracted. Details can be found in online material D6, including an explanation of differences compared to what is described in Weltevrede (2016).

Examples of 2DFSs are shown in panels (iii) and (iv) of Fig. 1. The vertical axis has the same unit as that of the LRFS, while the horizontal axis corresponds to the fluctuation frequency $1/P_2$ in cpp. For drifting subpulses, P_2 is the separation between drift bands in the pulse longitude direction. A visual aid to assess the asymmetry of a spectral feature in the 2DFS with respect to $1/P_2 = 0$ is the bottom panel attached to the 2DFS, which shows the vertically integrated power of the 2DFS between the dotted lines indicating the most relevant feature to assess the asymmetry for. When no such feature is identified, there are no dotted lines shown in the 2DFS, and the full spectrum is integrated over. To highlight any asymmetry, a mirrored curve is shown as the dashed line. In the case of PSR J1539−6322 column (a) of Fig. 1, a 2DFS is produced for each of the two profile components. The subpulses for both components have positive drifting directions (subpulses drift towards the trailing side of the profile), corresponding to the power in the 2DFS peaking at a positive $1/P_2$ frequency.[6] The spectral features peak at $1/P_2 \simeq 30$ and $\simeq 60$ cpp for the leading and trailing components, respectively, corresponding to $P_2 \simeq 360^\circ/30 = 12^\circ$ and 6°. The first profile component shows a weaker spectral feature with the $1/P_3$ and $1/P_2$ frequencies doubled, as expected for the first harmonic of the drifting subpulse feature.

Column (b) of Fig. 1 (for PSR J1539−4828) shows an example of a broad spectral feature close to the alias boarder at $1/P_3 =$ 0.5 cpp. The vertical extension of the spectral feature indicates that the modulation periodicity P_3 is variable. When $P_3 < 2$, the sampling of the pattern once per pulse period is not enough to resolve the periodicity unaliased. As a result, a periodicity slightly faster than 2 will be observed slightly slower than 2 with a drift direction that is opposite. Indeed, the 2DFS shows spectral features at ±60 cpp suggestive of opposite apparent detected drift directions. In this example, negative drift dominates over positive drift.

[6]Following Weltevrede et al. (2006, 2007), the 2DFS is mirrored about the vertical axis to ensure that positive drift corresponds to a positive $1/P_2$ frequency.

2.3.4 Shuffle-normalized spectra

There are two contributions to the uncertainty in the found spectral features. One is attributed to the (possibly white) system noise. However, for most analysed pulsars, the significance of features is limited by the finite number of pulses. This can make a spectral feature spurious rather than reproducible in longer observations. What we will refer to as 'shuffle-normalized spectra' (both the LRFS and 2DFS) are constructed to assess whether a spectral feature is significant or not.

Spectra are computed for 1000 pulse sequences where the order of pulses is randomized, resulting in an average spectral power and root mean square (rms) for each spectral bin. No significant structures in $1/P_3$ are expected in the spectra of the randomized pulse sequences. The shuffle-normalized spectra are calculated such that for each bin in the original spectrum the average power is subtracted, before dividing by the rms. In addition, any spectral bins for which the power in the original spectrum does not exceed two times the off-pulse spectral rms are set to zero. The resulting shuffle-normalized spectra highlight spectral features associated with organized subpulse modulation and suppress stochastic subpulse variability.

Examples of shuffle-normalized spectra are shown in column (d) of Fig. 1. These have identical markings of the P_2 and P_3 measurements, and $1/P_3$ ranges associated with each spectral feature, compared to the regular spectra (column c). The regular LRFS (panel c ii) is dominated by variability associated with the main part of the pulse profile between pulse longitude ∼250° and ∼270°, with a hint of a broad (diffuse) excess of spectral power between 0.1 and 0.3 cpp. In contrast, the shuffle-normalized LRFS (panel d ii) reveals a much sharper spectral feature at ∼0.08 cpp associated with the very low intensity leading part of the pulse profile (between pulse longitude 220° and 250°). This is a clear demonstration of the power of the shuffle-normalized spectra. The weak spectral features, corresponding to organized subpulse modulation, stand out more clearly by suppressing spectral power associated with stochastic pulse-to-pulse variability. Also, in the first 2DFS (corresponding the leading part of the profile) the spectral feature is clearer in the shuffle-normalized spectrum. This spectral feature corresponds to the subpulse modulation reported by Kou et al. (2021). Appendix B has more details related to shuffle-normalized spectra. All the regular and shuffle-normalized spectra can be found in the online material.

2.3.5 2DFS analysis

The spectra of all pulsars were investigated for evidence of significant spectral features. Identified features in the 2DFS are classified to be a drifting subpulse feature if there is a significant offset of the feature with respect to the $1/P_2$ axis. If no such offset is found, but there is a spectral feature that peaks at a specific non-zero $1/P_3$, this is defined as a P_3-only feature. For example, the spectral feature in panel (d iii) of Fig. 1 is classified as a P_3-only feature, while that in panel (d iv) is classed as a drifting subpulse feature.

Finally, there are three pulsars (PSRs J0905−5127, J1835−1106, and J1856+0113) where subpulse modulation is identified with a specific P_2 separation between subpulses, but without any phase relation of subpulses between successive pulses. For example, panel (e iii) in Fig. 1 shows two symmetrical vertical bands of power centred at $1/P_2 = \pm 150$ cpp, attributed to subpulses appearing with a typical separation within the pulse of $\sim 360^\circ/150 \simeq 2.4^\circ$. There is no significant structure in the $1/P_3$ direction as the pulsar has no memory of at which pulse longitude the subpulses appeared in the previous pulse. As a consequence, these spectral features disappear in the shuffle-normalized spectra (see online material). Besides this main spectral feature that is classified as a P_2-only feature, there is a weak drifting subpulse feature with $1/P_2$ at around −50 cpp with a $1/P_3$ around 0.2–0.3 cpp.

The spectra were inspected by eye for features of interest and for each pulsar the dominant feature was identified. The dominant feature is what is used in the statistical analysis when spectral properties of different pulsars are compared. See Appendix B for details, including how the significance of spectral features is assessed.

Weltevrede et al. (2006, 2007) classified drift subpulse features as either 'coherent' or 'diffuse' depending on the width of the spectral feature in $1/P_3$. Rather than judging this by eye, in this work the width of the feature is measured from the horizontally integrated spectral power of the 2DFS over the selected $1/P_2$ range for the feature. To suppress any excess spectral power not associated with the feature of interest, a similar approach to produce the shuffle-normalized spectra is used. However, here the average power of the spectra arising from the shuffled pulse sequences is subtracted, but the spectra are not normalized. This step helps suppressing the 'baseline' of the resulting integrated spectrum. An example of a shuffle-subtracted spectrum can be found in Appendix B, as well as further details related to this baseline subtraction. The resulting spectral power as a function of spectral bin i is $\mathcal{P}_i$. The variance associated with the width of the spectral feature is defined as

$$\sigma^2_{1/P_3} = \frac{\sum_i \mathcal{P}_i \times ((1/P_3)_i - \mu_{1/P_3})^2}{\sum_i \mathcal{P}_i}, \tag{2}$$

where $(1/P_3)_i$ is the frequency (in cpp) associated with spectral power $\mathcal{P}_i$, and the mean spectral frequency of the feature is defined as

$$\mu_{1/P_3} = \frac{\sum_i \mathcal{P}_i \times (1/P_3)_i}{\sum_i \mathcal{P}_i}. \tag{3}$$

In equations (2) and (3), the summation is only over the $1/P_3$ region covering the feature. The quoted values of σ_{1/P_3} are set to be at least the spectral resolution if the feature is unresolved. An error on σ_{1/P_3} is derived by repeating the computation many times after adding random Gaussian noise to the 2DFS with an rms equal to that measured in the off-pulse spectrum.

The spectral shape of a drift feature can be distinctly non-Gaussian. An advantage of the used method to measure the spectral width is that no fitting is involved, and that no specific spectral shape has to be assumed. When the spectral shape is non-Gaussian, the reported standard deviation does not fully quantify the shape of the spectral feature, but it is indicative of its width. Similarly, this procedure of subtracting the baseline from $\mathcal{P}_i$ is a relatively simple, but in general an effective way to isolate the spectral feature of interest. The main advantage of the methodology used is that no detailed modelling of the 2DFS is required, which is difficult to automate for a large number of pulsars.

Also, the strength of the spectral power associated with drifting subpulses is quantified with a procedure that does not rely on fitting the spectral shapes of features in the 2DFS. This is done by quantifying the overall asymmetry of spectral power $\mathrm{2DFS}_{i,j}$ in the 2DFS, defined as

$$P_{\rm asym} = \frac{|\sum_j \sum_i (\mathrm{2DFS}_{i,j} - \mathrm{2DFS}_{i,j'})|}{\sum_i \sum_j (\mathrm{2DFS}_{i,j} + \delta_{j,j'} \mathrm{2DFS}_{i,j'})}. \tag{4}$$

Here, index i covers the full spectral range $1/P_3$ (so between 0 and 0.5 cpp), while j covers half of the range corresponding to $1/P_2$ (e.g. only positive frequencies). The index j' is defined to correspond to a frequency $1/P_2$ with the same magnitude, but the opposite sign compared to that of index j. The Kronecker delta $\delta_{j,j'}$ ensures that the spectral bin corresponding to $1/P_2 = 0$ (for which $j = j'$) is not double counted. The $1/P_2$ Nyquist frequency, which per definition is not associated with a drift direction, does not contribute to the numerator of equation (4), but is included in the denominator.

Equation (4) defines the fraction of subpulse modulation that is associated with an excess of drift in one particular direction. It is defined as a positive quantity, given that the numerator contains the absolute value of the difference in spectral power between the two halves of the 2DFS. The sign of the numerator of equation (4), without taking the absolute value, defines which drift direction dominates in the spectrum. The presence of noise (system noise as well as stochastic pulse-shape variability) implies that always some asymmetry can be expected in the 2DFS. The significance of the asymmetry is quantified by randomizing (shuffling) the order of the pulses many times and recomputing $P_{\rm asym}$. After shuffling, no significant drift can be expected; hence, the standard deviation of the obtained values of $P_{\rm asym}$ quantifies its uncertainty.

AN S/N bias is introduced in equation (4) because the absolute value of the numerator is used. To quantify the bias, a few pulsars with drifting subpulses for which high-S/N observations were available were analysed further. Different amounts of white noise were added to the pulse stack and $P_{\rm asym}$ was recalculated. If the S/N $\gtrsim$ 100, no significant bias is observed. For the statistical analysis related to $P_{\rm asym}$, only observations with an S/N above 100 are considered to minimize this bias (see Section 5.3).

2.4 P–$\dot{P}$ correlation analysis

How the quantities derived from the spectral analysis vary as a function of P and $\dot{P}$ is investigated in Section 5. The correlations between a measured quantity F (e.g. P_3) and a combination of P and $\dot{P}$ are parameterized as

$$\log_{10} F = c(\log_{10}(P^a \dot{P}^b))^2 + d \log_{10}(P^a \dot{P}^b) + e. \tag{5}$$

The constants a and b define the direction in the P–$\dot{P}$ diagram, and the quadratic form parameterized with the constants c, d, and e allows a non-linear variation to be described. Where a linear relation is observed in the P–$\dot{P}$ diagram, c can be fixed at zero. The ratio a/b, or b/a, defines a gradient in $\log_{10}(P)$–$\log_{10}(\dot{P})$ space; hence, a and b are not independent parameters. Therefore, when fitting equation (5), either a or b is set to 1. Unless the correlation is dominated by a dependence on P or $\dot{P}$, the choice of which parameter to keep as a free parameter is arbitrary, but is informed by which resulted in more Gaussian-like posterior distributions or a larger correlation coefficient (see below). Under the assumption of energy loss via magnetic dipole radiation, characteristic age $\tau_{\rm c}$, kinetic energy loss rate $\dot{E}$, and the dipolar component of the surface magnetic field strength B correspond to $a/b = -1$, -3 and $+1$, respectively. The true age and surface magnetic field strength can be significantly different from the derived $\tau_{\rm c}$ and B, e.g. in the presence of other energy-loss mechanisms.

The best-fitting parameters are determined by a Bayesian Markov chain Monte Carlo (MCMC) approach. In addition to the parameters

Table 1. Pulsars for which P and $\dot{P}$ were corrected (as shown) to a harmonic.

Pulsar	Harmonic	P (s)	$\dot{P}$ (s s^{-1})
J0211−8159	3	3.2	8.7×10^{-16}
J0711+0931	2	2.4	8.0×10^{-16}
J0836−4233	2	1.5	2.6×10^{-15}
J1427−4158	2	1.2	1.2×10^{-15}
J1618−4723	2	0.41	4.0×10^{-15}
J1639−4604	2	0.53	5.8×10^{-15}
J1714−1054	3	2.1	1.8×10^{-16}
J1739−3951	2	0.7	4.0×10^{-17}
J1802+0128	2	1.1	4.2×10^{-15}
J1830−0131	3	0.46	6.3×10^{-15}
J1848−1150	2	2.6	2.9×10^{-15}
J1946−1312	2	1.0	4.0×10^{-15}

in equation (5), an extra noise term σ_e is included. This accounts for a non-perfect correlation, even after accounting for the measurement uncertainties. Details of the fitting process can be found in online material D7.

To assess the significance of the found correlations, a weighted correlation coefficient between the measured $\log_{10}F$ values and the model (equation 5) is calculated. The data are weighted down by a variance equal to the quadrature sum of the measurement error and σ_e. The uncertainty on the correlation coefficient is estimated using bootstrapping, whereby the correlation coefficient is repeatedly recalculated using randomly selected samples with replacement from the whole data set, after applying offsets drawn from a Gaussian distribution with a standard deviation set to the measurement error. The standard deviation of the distribution of correlation coefficients is taken to be the uncertainty on the measured correlation coefficient.

3 THE SAMPLE AND A SURVEY COMPARISONS

3.1 The sample

The observing strategy of the TPA project is defined in Song et al. (2021). This strategy ensures high-fidelity observations suitable for the detection of profile variability by taking into account the time required to achieve the desired profile stability. A pulsar monitoring campaign is currently being carried out, which adopts a strategy that exploits the ability of MeerKAT to form two subarrays. In addition, for the brightest half of the sample a longer pulse sequence (1024 or more pulses) was recorded using all available dishes from the MeerKAT array to maximize the sensitivity to detect individual pulses. Also, for many pulsars with a lower flux density more than 1024 pulses were recorded to reach the required sensitivity and profile stability (Song et al. 2021).

We here present the analysis of data for 1198 pulsars. For the majority of pulsars (887), an observation of at least 1024 pulses is used. See online material D8 for a more detailed description of the distribution of observation lengths.

A comparison between the measured S/N of the integrated pulse profiles and that aimed for using the methodology of Song et al. (2021) shows that for many pulsars (for 762 out of 1060) the S/N of the data is consistent with the expected S/N within a factor of 2 (see online material Fig. D3). Reasons why the S/N is lower than expected include that for some pulsars their actual flux densities (see Posselt et al. 2022, for our TPA measurements) are different compared to the catalogued values assumed (see Song et al. 2021, for a discussion), RFI, and the use of the less sensitive subarray observations in 26 cases. Subarray observations were used for various reasons, including technical faults, less favourable interstellar scintillation, or nulling conditions. The level of deviation is consistent with the findings of Song et al. (2021).

A consequence of the spread in S/N is that not all observations are equally sensitive in detecting drifting subpulses, and this will be further discussed in Section 4. Furthermore, the S/N is correlated with other pulsar parameters, in particular, with pulse period P such that long-period pulsars typically have a somewhat higher S/N (see online material Fig. D4). This is because long-period pulsars were observed with longer observing length t_{obs}, since the majority of pulsars in the sample (763 out of 1198) were observed for ∼1000 pulses. So higher S/Ns ($\propto \sqrt{t_{obs}}$) are observed for longer period pulsars. Also, the duty cycle W/P, where W is the pulse width, plays a role and is correlated with the spin parameters (Posselt et al. 2021). The S/N bias is further discussed in Sections 4 and 5.

Some of the statistical analysis relies on information (in particular the spin parameters) from the pulsar catalogue (ATNF catalogue[7] version 1.67; Manchester et al. 2005), except for PSR J1357−62 for which we used parameters supplied by S. Johnston (priv. comm.). For two pulsars, we used the name from the pulsar catalogue (PSRs J0514−4408 and J1402−5021) rather than the name used when the data were recorded (PSRs J0514−4407 and J1402−5124).

In addition, 12 pulsars were identified to be folded at a harmonic of the true pulse period, implying that the pulse period in the catalogue was incorrect. This resulted in very sharp spectral features in our analysis. The data (after correcting both P and $\dot{P}$) were refolded, as summarized in Table 1.

Within the sample of pulsars, there are 30 showing evidence of severe scattering with a time-scale comparable to or longer than the pulse widths. These pulsars were visually identified, and included a subsample of those studied in Oswald et al. (2021). For some of them, the large duty cycles are problematic (see Sections 2.3.2 and 2.3.3). Therefore, these pulsars are excluded from analysis where relevant (see Section 5).

3.2 Comparison with other surveys

The main table summarizing our measurements can be found in the online material, of which the first entries are also in Table 2. The spectral figures are in the online material as well, with Fig. 1 being an example. Before analysing their statistical properties, the performance of the employed analysis techniques (Section 2) is assessed first. This is done by comparing our results for individual sources with those obtained by Weltevrede et al. (2006) and Basu et al. (2016, 2019). This comparison gives an indication of the completeness and accuracy of our analysis.

Weltevrede et al. (2006) analysed 187 pulsars using the WSRT data at an observing frequency comparable to the data presented here and 116 pulsars were in both surveys. In addition, a comparison is made with the results of Basu et al. (2016, 2019), who analysed a combined data set of 123 pulsars observed with GMRT at a lower frequency of 618 and 333 MHz. Basu et al. (2019) analysed a larger sample compared to Basu et al. (2016), but with a focus on phase modulations only. They reported 61 pulsars with drifting subpulses, of which 49 pulsars are covered in our sample. In online material D9, we report on the small fraction of the sample for which our results do not confirm the reported results, or for which we detect not-reported

[7] http://www.atnf.csiro.au/research/pulsar/psrcat

Table 2. The first few entries of the table that can be found in the online material summarizing the spectral subpulse modulation measurements. For each pulsar's P and $\dot{P}$, as well as the τ_c and $\dot{E}$ derived from these, are reported. This is followed by the number of pulses used for the modulation index analysis and the corresponding S/N. The parameters $\bar{m}$, $P_{\rm asym}$, P_2, P_3, and σ_{1/P_3} are defined in Sections 2.3.2 and 2.3.5. Each pulsar can have multiple profile components, each of which can have multiple spectral features. Each feature is assigned a class (drift/P_3-only/P_2-only correspond to drifting subpulses, P_3-only, or P_2-only features, respectively, as defined in the main text). A more in-depth description of the parameters is provided with the full online table.

PSRJ	PSRB	P (s)	$\dot{P}$ (10^{-15} s s^{-1})	τ_c (10^5 yr)	$\dot{E}$ (10^{33} erg s^{-1})	Pulses	S/N	$\bar{m}$	$P_{\rm asym}$ (per cent)	Class	Comp	P_3	σ_{1/P_3} (cpp)	P_2 (deg)
J0034−0721	B0031−07	0.943	0.408	366.0	0.019	1040	1985	1.458(1)	−15.0(7)	drift	MP C1	**6.6(2)**	0.010(4)	-23^{+3}_{-11}
										drift	MP C1	9.9(7)	0.015(6)	-23^{+2}_{-64}
J0038−2501	–	0.2569	0.001	53 600.0	0.002	2336	73	2.01(9)	38(16)	–	–	–	–	–
J0045−7042	–	0.6323	2.49	40.2	0.389	1632	36	1.6(2)	−13(15)	–	–	–	–	–
...														

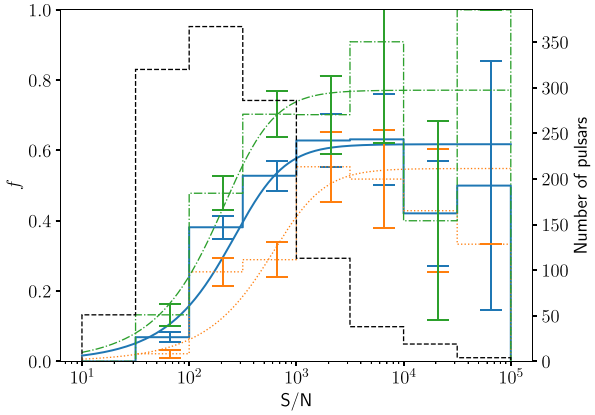

Figure 2. Distribution of the fraction of pulsars with drifting subpulses f (solid histogram), with error bars corresponding to the square root of the number of pulsars with drifting subpulses divided by the total number of pulsars in a given S/N bin (dashed histogram). The solid curve is the fit of f with equation (6). The dotted and dash–dotted f distributions (fitted with the same functional form) correspond to pulsars with τ_c below and above the median τ_c of the sample.

subpulse modulation. In addition, we comment on the minority of pulsars in the overlapping samples for which the P_3 measurements are inconsistent.

4 THE FRACTION OF PULSARS WITH DRIFTING SUBPULSES

Of the total 1198 pulsars in our sample, we found evidence for drifting subpulses in 418 pulsars, which corresponds to 35 per cent. As pointed out by, for example, Weltevrede et al. (2006), the detectability of drifting subpulses depends on the S/N of the observation, so the intrinsic fraction of pulsars with drifting subpulses must be higher. This is demonstrated in Fig. 2, which shows the fraction of pulsars with drifting subpulses (solid histogram) as a function of the S/N of the integrated pulse profile of the observation. It is evident that at low S/N, drifting subpulses are less likely to be detected. The fraction of pulsars with drifting subpulses f increases strongly towards higher S/N, before the distribution flattens at around $f = 0.6$ when the S/N exceeds ∼1000.

The observed distribution f has a functional shape comparable to what can be used to describe high-pass filters, and is fitted as

$$f = f_\infty \frac{(\mathrm{S/N})/(\mathrm{S/N})_0}{\sqrt{1 + ((\mathrm{S/N})/(\mathrm{S/N})_0)^2}}, \quad (6)$$

where f_∞ is the fraction of pulsars with detectable drifting subpulses in the limit of high S/N, and $(\mathrm{S/N})_0$ quantifies the location of the turnover in the distribution where $f = f_\infty/\sqrt{2}$. The observed distribution is well described with this function with the fitted parameters $f_\infty = 0.62 \pm 0.08$ and $(\mathrm{S/N})_0 = 400 \pm 100$ (solid blue curve in Fig. 2). For many observations, S/N < $(\mathrm{S/N})_0$ (see the dashed black distribution in Fig. 2). This highlights that the 35 per cent of pulsars with detectable drifting subpulses severely underestimate the intrinsic fraction of pulsars with drifting subpulses, which is better estimated as f_∞. This is consistent with the statement by Weltevrede et al. (2006) that over half of all pulsars would have detectable drifting subpulses in high enough S/N data, although the sample studied here is large enough to show that even for observations with very high S/N drifting subpulses are not detectable in all pulsars. When P_3-only pulsars are included in f, the plateau would be slightly higher with $f_\infty = 0.72 \pm 0.06$.

One should be careful with interpreting the dependence of f with S/N, as the S/N of the observations is correlated with P (see Section 3). Not only are high-S/N data beneficial for the detectability of drifting subpulses, long-period pulsars (with higher S/N) are intrinsically more likely to show drifting subpulses since they are associated with large τ_c (e.g. Rankin 1986; Weltevrede et al. 2006, but see also Section 5.3). To disentangle these two effects, f as a function of S/N was considered for pulsars with τ_c below and above the median value of 4.6×10^6 yr (shown as the dotted orange and dash–dotted green distributions in Fig. 2). For both age groups, f increases with S/N, and older pulsars are more likely to show drifting subpulses. Fitting of equation (6) reveals that the turnover $(\mathrm{S/N})_0$ is similar for all distributions, suggesting that the dominant aspect to the S/N dependence of f is the observational bias making drifting subpulses easier to detect when the S/N is high. The pulsar luminosity is observed to be uncorrelated with f, demonstrating that the physical parameters governing the radio luminosity do not contribute to the detectability of drifting subpulses in pulsars.

Apart from S/N, there are other factors that affect the detectability of drifting subpulses. For some pulsars, drifting subpulses can be highly regular, making them easier to detect. For others, the drifting subpulse patterns are highly irregular, potentially interrupted by nulling or intervals of time corresponding to an emission mode where there are no detectable drifting subpulses. The length of the observations analysed here is in general sufficiently long to allow the detection of drifting subpulses, and the length is found to be uncorrelated with f (not shown).

Our results confirm that drifting subpulses are a very common phenomenon for radio pulsars; hence, the physical conditions required for the production of drifting subpulses cannot be very different compared to the required conditions for the radio emission mechanism itself. Drifting subpulses might well be a fundamental property of the emission mechanism, although they are not detectable

Table 3. A summary of the correlations found (see Section 5) for the subpulse modulation properties (first column) with P and $\dot{P}$. The next two columns explain if a/b (b is fixed to 1) or b/a (a is fixed to 1) is fitted for and the result, and if c is fixed at zero in equation (5). The final two columns show the strength of correlation quantified with the correlation coefficient, and whether it is consistent with evolution in the τ_c ($a/b = -1$), $\dot{E}$ ($a/b = -3$), P ($b = 0$), or $\dot{P}$ ($a = 0$) direction.

Property	Fit	$c = 0$	Correlation	Consistent
P_3	$a/b = -1.7 \pm 0.3$	N	0.34 ± 0.05	τ_c
σ_{1/P_3}	$a/b = -2.6 \pm 0.4$	N	0.36 ± 0.05	$\dot{E}$
$P_{\rm asym}$	$a/b = -1.8 \pm 0.4$	Y	0.30 ± 0.03	τ_c, $\dot{E}$
$\lvert P_2 \rvert$	$a/b = -5.5 \pm 2.0$	Y	0.46 ± 0.04	$\dot{E}$, τ_c, $\dot{P}$
$\lvert D \rvert$	$b/a = -0.2 \pm 0.1$	Y	0.20 ± 0.04	$\dot{E}$, P
$\lvert D \rvert/(W_{50}/2)$	$a/b = -1.1 \pm 0.5$	Y	0.32 ± 0.05	τ_c, $\dot{P}$
$\bar{m}$	$b/a = 0.03 \pm 0.06$	N	0.26 ± 0.04	P

for all pulsars. The origin of the dependence of f with the spin parameters is explored in more detail in Section 5.

5 SUBPULSE MODULATION IN P–$\dot{P}$ SPACE

In this section, we quantify the evolution of subpulse modulation in the P–$\dot{P}$ diagram, with a focus on properties related to drifting subpulses. The best-fitting P and $\dot{P}$ relations (using the MCMC method described in Section 2.4) are summarized in Table 3, including the strength of the correlation. Different properties are discussed in turn, aimed at building a phenomenological understanding of how subpulse modulation evolves in the P–$\dot{P}$ diagram. The found correlations are compared with an evolution with τ_c or $\dot{E}$ (see Table 3). It should be stressed that P, $\dot{P}$, τ_c, and $\dot{E}$ are not independent parameters. However, these are useful parameters to relate the measurements to emission models. The qualitative interpretations are described geometrically in terms of the carousel model. Nevertheless, they could apply to any model capable of producing periodic subpulse modulation. The properties presented here will be further explored and compared to predictions in Section 6.

5.1 P_3 evolution

Before exploring how pulsars with drifting subpulses are distributed in P–$\dot{P}$ space, it is instructive to consider the evolution of P_3 first. Many pulsars have multiple measured P_3 values. This could be because there are multiple profile components with separate P_3 measurements (this is discussed in Section 6.4), or multiple periodicities were identified in a given component. Here, we analyse a single P_3 for each pulsar, identified to be the dominant drifting subpulse feature by virtue of being the strongest and most striking. Preference is given to more well-defined (narrow) features. The used P_3 values are bold in Table 2 and the corresponding online table. Pulsars severely affected by scattering were excluded.

The distribution of P_3 in the P–$\dot{P}$ diagram (Fig. 3) is V-shaped such that large P_3 values are found for the more energetic (large $\dot{E}$) and young (small τ_c) pulsars, as well as the least energetic old pulsars. At around $\tau_c \simeq 10^{7.5}$ yr (or $\dot{E} \simeq 10^{31.5}$ erg s^{-1}), the smallest P_3 values dominate. A strong correlation (see also Table 3) was found, such that the evolution is consistent with a dependence on τ_c and preferred over an evolution in the $\dot{E}$ direction. This V-shaped evolution of P_3 is further illustrated in Fig. 4 (solid line), which shows the evolution of the weighted mean P_3 in the direction in the P–$\dot{P}$ diagram suggested by the fit. The simulated distribution (dashed line) is computed by generating the same number of P_3 values as the original data from the fitted function (equation 5) with the best-fitting P–$\dot{P}$ combination.

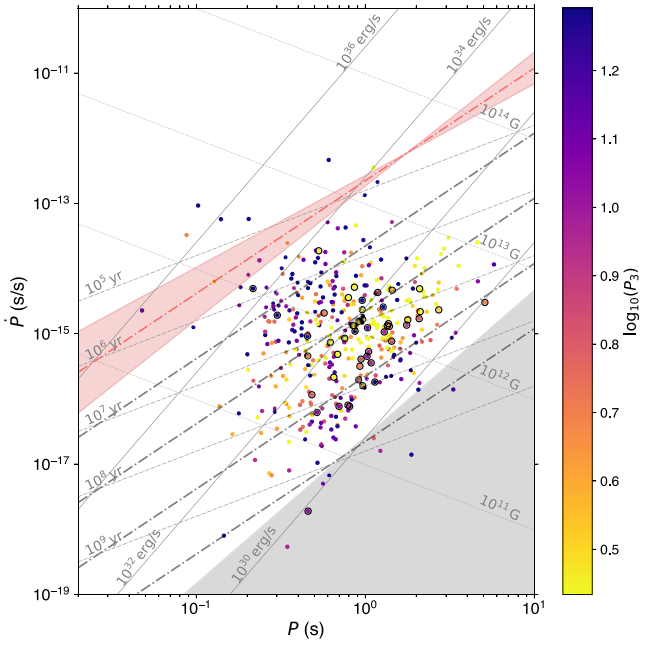

Figure 3. P–$\dot{P}$ diagram where the colours of the dots represent $\log_{10}(P_3)$ for each pulsar with a dominant drifting subpulse feature identified. Pulsars that have multiple distinct P_3 measurements for a single profile component are marked with black circles. The dot–dashed lines correspond to constant P_3 values according to a fit of equation (5) (with $b = 1$). The top shaded region indicates the 1σ uncertainty on the slope. Lines of constant τ_c, B, and $\dot{E}$ are shown as the double dot–dashed, dotted, and solid lines, respectively. The region below the death line (equation 4 of Zhang, Harding & Muslimov 2000) is shaded in the bottom right corner.

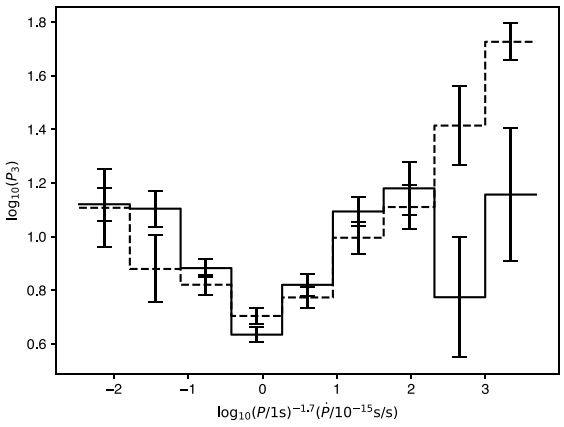

Figure 4. A histogram of the measured (solid) and predicted (dashed) weighted mean P_3 as a function of the combination in P and $\dot{P}$ corresponding to the direction of the strongest correlation in the P–$\dot{P}$ diagram. The prediction is based on equation (5) fitted to the measured distribution. The error bars represent the standard deviation of values contributing to each bin, divided by the square root of the number of values.

Each P_3 value is generated from a Gaussian distribution with mean of the corresponding predicted value from the fitted function and a standard deviation as the combined error of the scatter of points σ_e and the measurement error. This shows that the fit can reproduce the found evolution.

Near $\tau_c \simeq 10^{7.5}$ yr ($\dot{E} \simeq 10^{31.5}$ erg s^{-1}), many pulsars have P_3 values relatively close to the alias border $P_3 = 2$. This suggests that

the V-shaped evolution is a consequence of aliasing, arising from the emission pattern being observed once per stellar rotation. In the geometric framework of a carousel model, this could be caused by a monotonic evolution of the carousel rotation period. The oldest and least energetic pulsars have slowly rotating carousels resulting in large unaliased P_3 values. For somewhat younger pulsars, the rotation is faster leading to a decrease in P_3. Even faster carousels for even younger pulsars then ultimately allow for aliasing to occur, such that the apparent P_3 can be large again despite that intrinsically now $P_3 < 2$ (this will be quantified in Section 6.2). Although described in the framework of a carousel model, the aliasing effect could apply to any model that can produce periodic subpulse modulation.

Pulsars with multiple P_3 features in a single profile component are marked in open circles in Fig. 3, which could be a consequence of drift mode changes. The majority of these are relatively old low-$\dot{E}$ pulsars. The number of these pulsars is too small to impact the conclusions related to P_3 evolution depending on which of the multiple P_3 measurements are used for a given pulsar, and the V-shaped evolution persists when the smallest P_3 is selected instead of the dominant feature.

Fig. 3 is for the 403 pulsars for which the dominant spectral feature is associated with drifting subpulses. The distribution for the 130 pulsars for which the dominant spectral feature is a P_3-only feature is more uniform throughout the pulsar population without evidence for a similar evolution (see Fig. C1). Very different distributions are to be expected, as at least some of the P_3-only features will be related to a time-scale associated with nulling or mode changing, which can have a distinctly different origin (e.g. Rankin 1986; Basu, Mitra & Melikidze 2020). This also explains the significantly different mean P_3 values for pulsars with drifting subpulses compared to P_3-only pulsars, as confirmed by Student's t-test giving a P-value of 4×10^{-8}.

5.2 Spectral width evolution

As discussed in Weltevrede et al. (2006), older pulsars tend to exhibit more 'coherent' drifting subpulses, corresponding to better defined P_3 values, while the spectral features of younger (or high-$\dot{E}$) pulsars are more 'diffuse'. In our work, the spectral width σ_{1/P_3} in the $1/P_3$ direction quantifies the coherency of the drifting subpulses, thereby allowing a more detailed investigation compared to a binary coherent/diffuse classification in Weltevrede et al. (2006). The P–$\dot{P}$ diagram in Fig. 5 shows σ_{1/P_3} for the dominant drifting subpulse feature, revealing that the most coherent subpulse modulation is indeed found for the oldest pulsars.

The found evolution (see Table 3) is close to an evolution in the $\dot{E}$ direction, and is preferred over an evolution in τ_c direction. A histogram of the spectral width (Fig. C2) shows that its evolution starts to flatten for $\dot{E} \gtrsim 10^{32}$ erg s^{-1}. This flattening is why a parabolic fit is preferred, rather than there being evidence for a turnover in the evolution.

It is suggested that pulsars with smaller τ_c have faster intrinsic modulation (Section 5.1), possibly because of faster rotating carousels. Therefore, instabilities in their modulation period could have a larger effect on the observed spectral width. This is especially the case if their modulation is aliased, as this will amplify the apparent diffuseness of the spectral features compared to the intrinsic instability of the periodicities. The spectral width evolution therefore supports our suggestion that the youngest pulsars have aliased P_3, rather than the oldest. The spectral width appears to be stronger linked to $\dot{E}$ than τ_c, while the opposite is true for the P_3 evolution. This implies that P_3 and σ_{1/P_3} are not both associated with only

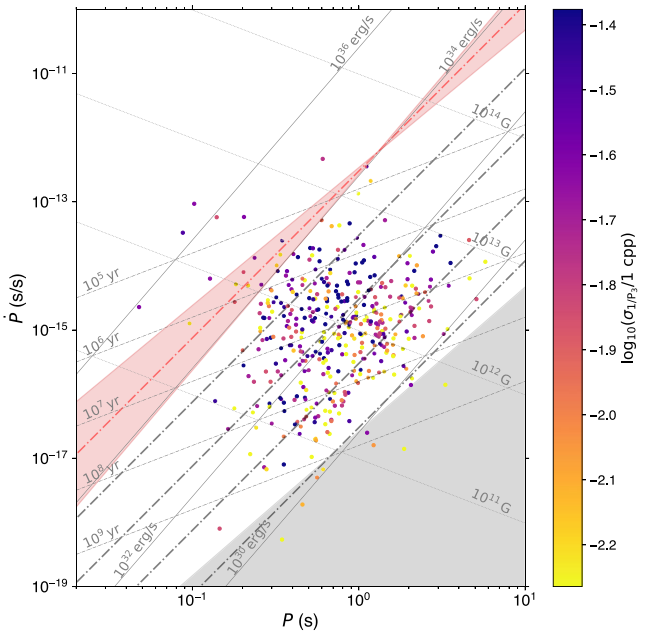

Figure 5. P–$\dot{P}$ diagram where the colours of the dots represent σ_{1/P_3} for each pulsar with a dominant drifting subpulse feature identified. The dot–dashed lines correspond to constant σ_{1/P_3} values according to a fit of equation (5) (with $b = 1$). The top shaded region indicates the 1σ uncertainty on the slope. See the caption of Fig. 3 for further details.

τ_c or $\dot{E}$. Nevertheless, the P–$\dot{P}$ evolution of P_3 and σ_{1/P_3} could be consistent with a common different combination of P and $\dot{P}$.

In Fig. 5, the P_3-only pulsars are excluded, as that sample includes modulation caused by, for example, nulling (see Section 5.1). Indeed, the mean σ_{1/P_3} values are different for P_3-only and drifting subpulse pulsars as confirmed with a Student's t-test with a P-value of 0.0002.

5.3 Detectability and strength of drifting subpulses

As shown in Fig. 6, pulsars with detected drifting subpulses (stars) are close to the death line. They therefore typically have larger τ_c and lower $\dot{E}$ than pulsars without detectable periodic subpulse modulation (dots). The τ_c distributions of these two populations are distinctly different, as the Kolmogorov–Smirnov test gives a P-value of 2×10^{-19}. This result confirms the finding of Ashworth (1982), Rankin (1986), Weltevrede et al. (2006), and Basu et al. (2016, 2019) in our much larger sample. Pulsars with P_3-only features, shown with diamonds in Fig. 6, are more spread out across the population. This is consistent with the findings in Basu et al. (2020), who found that pulsars with P_3-only features are found across a wide range of $\dot{E}$.

The preference for drifting subpulses to be detected in older and less energetic pulsars suggests that when the pulsars age their drifting subpulses become stronger. To test this, the evolution of $P_{\rm asym}$ (equation 4) is considered. This quantifies the asymmetry in the 2DFS arising when subpulses preferentially arrive earlier (or later) in successive pulses, and is independent of the spectral power being concentrated in a well-defined P_3 feature. Because it is especially not significantly biased by the S/N until S/N < 100 (see Section 2.3.5), unlike the detectability of drifting subpulses (see Section 4), this is a useful quantity to consider. This quantity is determined for all pulsars, regardless whether drifting subpulses are detected. For pulsars with multiple components, hence different

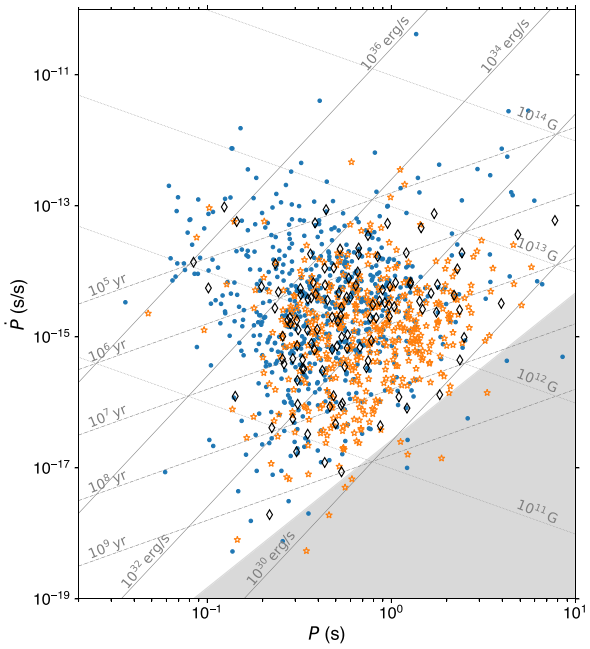

Figure 6. P–$\dot{P}$ diagram showing pulsars with detected drifting subpulses with stars, P_3-only pulsars with diamonds, and the other pulsars in the sample with the dots. See the caption of Fig. 3 for further details.

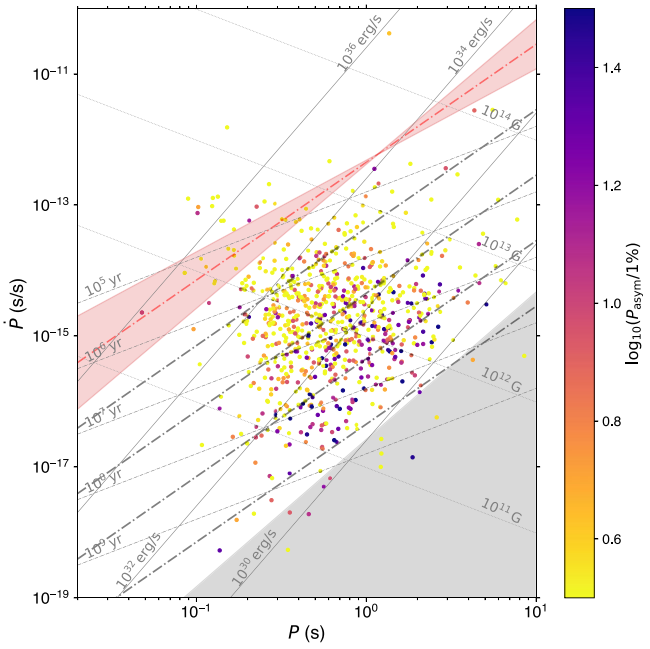

Figure 7. P–$\dot{P}$ diagram where the colours of the dots represent $P_{\rm asym}$ for the profile components for which $P_{\rm asym}$ has the smallest error bar. Only pulsars for which S/N $\geq$ 100 were considered. The dot–dashed lines correspond to constant $P_{\rm asym}$ values according to a fit of equation (5) (with $b = 1$ and $c = 0$). The top shaded region indicates the 1σ uncertainty on the slope. See the caption of Fig. 3 for further details.

$P_{\rm asym}$ measurements, the measurement with the smallest error bar is selected.

Fig. 7 shows the distribution of $P_{\rm asym}$ in the P–$\dot{P}$ diagram for pulsars with an S/N $\geq$ 100. A strong and significant (see Table 3) correlation is observed such that the older and less energetic pulsars tend to have the largest $P_{\rm asym}$. This confirms that strong drifting subpulse signals are associated with pulsars closer to the death line.

The directions of evolution of $P_{\rm asym}$ and P_3 in the P–$\dot{P}$ diagram are consistent (although the uncertainties are relatively large, see Table 3), suggesting that the same physical mechanism may be responsible for both. The transition between small and large values of $P_{\rm asym}$ occurs at $\tau_{\rm c} \simeq 10^7$ yr, which coincides with the transition from the smallest observed P_3 to larger values for the younger pulsars. The suggestion is made that younger pulsars are more likely to show aliased drifting subpulse patterns (Section 5.1), so the apparent drift direction of their subpulses is not necessarily constant throughout an observation. This would reduce $P_{\rm asym}$, and together with the increasing diffuseness of the spectral features (see Section 5.2) would reduce the detectability of drifting subpulses for younger pulsars. Although the decrease of $P_{\rm asym}$ for younger pulsars could in principle point to the emergence of stronger stochastic disorganized subpulses in that part of the P–$\dot{P}$ diagram, there is no evidence for such an evolutionary link from the analysis of modulation indices (Section 5.6).

5.4 Drift direction and P_2 evolution

The number of pulsars with positive and negative drift detected is 189 and 214, respectively. Here, positive drift corresponds to subpulses drifting from the leading to the trailing side of the pulse profile. So there is no preference for a drift direction in the pulsar population, thereby confirming the result of e.g. Weltevrede et al. (2006). From an MCMC analysis, no significant dependence on P and $\dot{P}$ is found. In the carousel model, the observed drift direction depends on whether there is an inner or outer line-of-sight cut through the emission beam. It can therefore be expected to be uncorrelated with the spin parameters.

Besides P_3, P_2 gives additional information about the appearance of the drifting subpulse patterns. Fig. 8 shows the distribution of $|P_2|$ for those pulsars with detected drifting subpulses. The population of pulsars with small $|P_2|$ values (lighter colour) is skewed towards the less energetic part of the population. Large $|P_2|$ values are preferentially found for the higher $\dot{E}$ pulsars, and also for the less energetic pulsars. Although the correlation is strong (see Table 3), the direction of evolution is relatively unconstrained. The Bayesian fitting (see Section 2.4) assumes a symmetric error. Since P_2 has asymmetric error bars, the error bar towards zero is chosen (i.e. the positive/negative error bar is chosen for positive/negative P_2 value). This is usually the larger error bar of the two, hence is the conservative choice.

In the geometric picture of a carousel producing the drifting subpulses, the larger $|P_2|$ for more energetic pulsars can be associated with a reduction of the number of beamlets in the carousel. The fact that less energetic pulsars tend to have small measured $|P_2|$ could result in spectral features in the 2DFS that are more clearly separated from the vertical axis. This will help to make drifting subpulses easier to detect for less energetic pulsars. An alternative reason for the larger $|P_2|$ values observed for more energetic pulsars would be additional disorganized subpulse modulation (with associated power along the vertical axis of the 2DFS) skewing the measured centroid position of the spectral features towards larger $|P_2|$.

It is suggested that the carousel should be rotating faster for more energetic pulsars to explain the P_3 evolution in the P–$\dot{P}$ diagram (Section 5.1), ignoring a possible evolution in the number of beamlets. Since P_3 quantifies the time for a subbeam to rotate over a subbeam separation, a reduction in the number of beamlets (increased

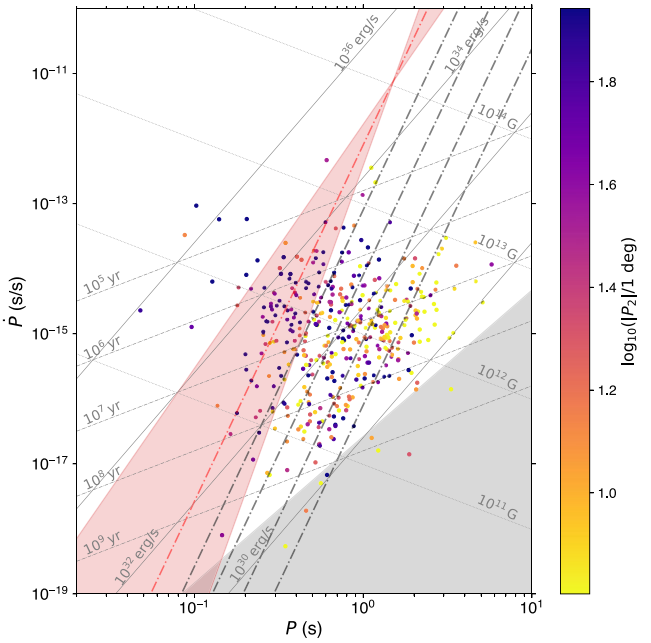

Figure 8. P–$\dot{P}$ diagram where the colours of the dots represent $|P_2|$ for each pulsar with a dominant drifting subpulse feature identified. The dot–dashed lines correspond to constant $|P_2|$ values according to a fit of equation (5) (with $b = 1$ and $c = 0$). The top shaded region indicates the 1σ uncertainty on the slope. See the caption of Fig. 3 for further details.

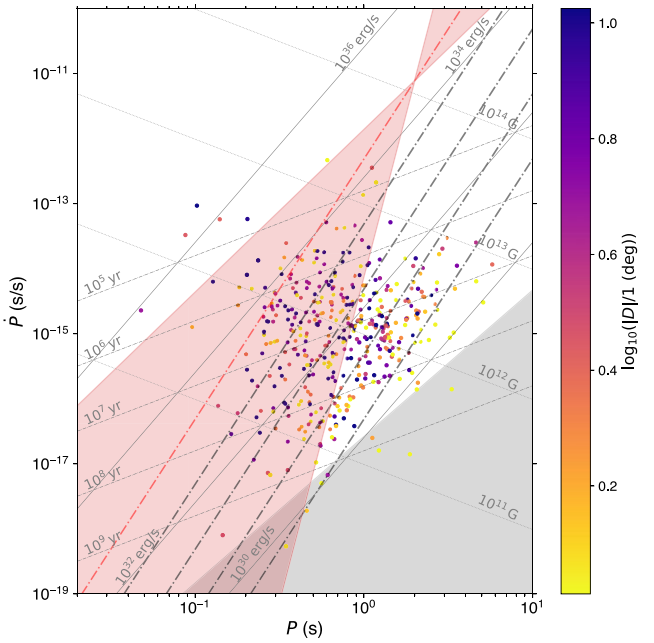

Figure 9. P–$\dot{P}$ diagram where the colours of the dots represent the drift rate for each pulsar with a dominant drifting subpulse feature identified. The dot–dashed lines correspond to constant $|D|$ values according to a fit of equation (5) (with $a = 1$ and $c = 0$).

separation) for energetic pulsars implies that an even faster carousel is required to compensate and explain the observed P_3 values.

For fast-rotating carousels, the beamlets could rotate appreciably during a time P_2, affecting the measured P_2 (Gupta et al. 2004). Depending on which hemisphere of the carousel is observed, its rotation is either with or against the rotation of the star, with opposite effects on the apparent P_2. Therefore, averaged over the population, this effect on P_2 is assumed to be cancelled out. In addition, an evolution of the magnetic inclination angle α could affect the measured P_2, but it will be argued in Section 6.3 that it would strengthen the statement that more energetic pulsars have faster carousels. In addition, it will be shown that the effect of pulse width evolution has no effect on this conclusion.

5.5 Drift rate evolution

The drift rate $|D| \equiv |P_2|/P_3$ does not provide independent information compared to what is discussed in Sections 5.1 and 5.4, but it is a useful quantity as it relates to the gradient of the drift bands. The drift rate distribution shows a relatively weak correlation in the P–$\dot{P}$ diagram (Fig. 9) such that less energetic older pulsars typically have smaller $|D|$. A relatively modest correlation is found (see Table 3), consistent with an absence of a correlation with $\dot{P}$.

The drift rate can be linked to how clear the drifting subpulse pattern is by comparing P_2 to the pulse width W. If a subpulse drifts over W in ∼two stellar rotations or less ($2|D| \gtrsim W$), it is visible for such a short time that a stable pattern of multiple beamlets is required for the drifting subpulses to be easily recognizable in a pulse stack. The pattern can therefore be more susceptible to being distorted, making the subpulse pattern more difficult to recognize in a pulse stack. To quantify this, the drift rate is normalized by $W_{50}/2$, where W_{50} is the full width at half maximum of the pulse profile as determined by Posselt et al. (2021). W_{50} varies across the population,

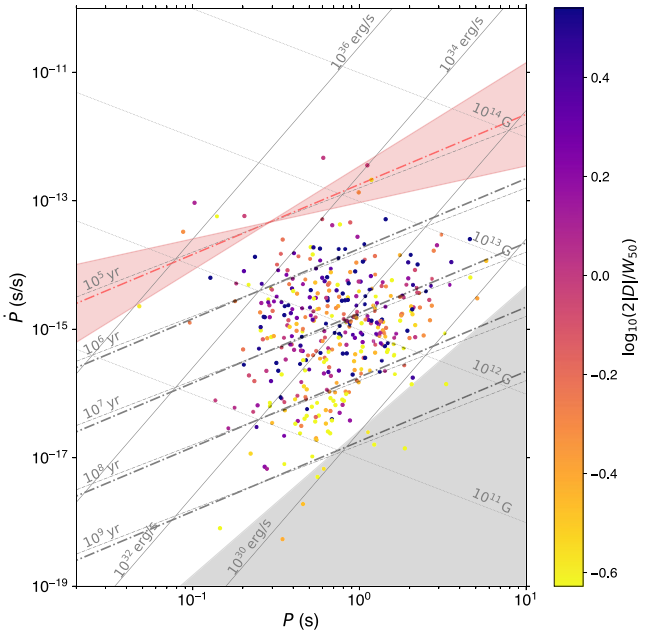

Figure 10. P–$\dot{P}$ diagram where the colours of the dots represent the drift rate normalized with $W_{50}/2$ for each pulsar with a dominant drifting subpulse feature identified. The dot–dashed lines correspond to constant $|D|$ values according to a fit of equation (5) (with $b = 1$ and $c = 0$). The top shaded region indicates the 1σ uncertainty on the slope. See the caption of Fig. 3 for further details.

such that younger pulsars tend to have wider profiles (e.g. Posselt et al. 2021).

The normalized drift rate is shown in Fig. 10, showing that a pulsar with a $\tau_c \gtrsim 5 \times 10^7$ yr ($\dot{E} \lesssim 5 \times 10^{32}$ erg s^{-1}) is more likely to have $|D| < W_{50}/2$. This corresponds well with the region in the

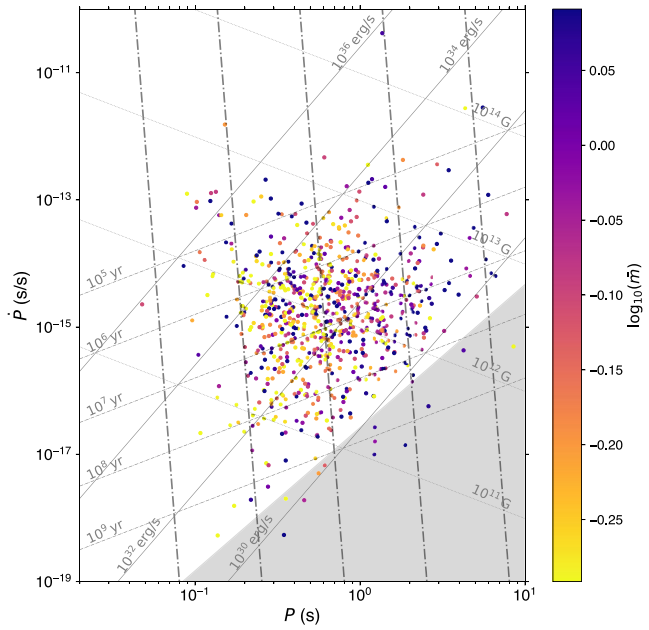

Figure 11. P–$\dot{P}$ diagram where the colours of the dots represent $\bar{m}$ of the MP for pulsars with an S/N > 100. The dot–dashed lines correspond to constant $\bar{m}$ values according to a fit of equation (5) (with $a = 1$). See the caption of Fig. 3 for further details. Given the large error bar, the direction of the correlation is not shown.

P–$\dot{P}$ diagram for which drifting subpulses are strongest and most often detected (Section 5.3). Some energetic younger pulsars can have small drift rates, but many do not. The correlation is modest, as summarized in Table 3.

5.6 Modulation index evolution

The average modulation index $\bar{m}$ quantifies the level of variability of single pulses (equation 1). When an IP is detected, only $\bar{m}$ corresponding to the MP is analysed here. Because $\bar{m}$ is biased such that it is lower at low S/N (see Section 2), only observations with an S/N > 100 are considered. In addition, pulsars with on-pulse regions that are so wide that no suitable off-pulse could be identified to subtract from the spectra are excluded as these $\bar{m}$ measurements will be biased high.

The $\bar{m}$ distribution in the P–$\dot{P}$ diagram (Fig. 11) shows a skew such that pulsars with $P > 1$ s have typically a large $\bar{m}$. The modest correlation is consistent with an absence of a correlation with $\dot{P}$. The significance of the quadratic term with $c = 0.12 \pm 0.05$ in equation (5) is less than 3σ, but quantifies the flattening at small P seen in the distribution in Fig. C3. The $\bar{m}$ evolution appears to be distinctly different in the P–$\dot{P}$ diagram compared to the detectability of drifting subpulses.

Evidence of strong subpulse modulations in long-period pulsars has been reported in the literature. For example, the radio magnetar XTE J1810−197 (PSR J1809−1943 in our sample) (Serylak et al. 2009; Levin et al. 2019) and the recently discovered 75 s pulsar J0901−4046 (Caleb et al. 2022) show clear and strong single-pulse shape variations, resulting in large modulation indices. On the other hand, some long-period pulsars and magnetars, e.g. the 23.5 s pulsar J0250+5854 (Tan et al. 2018), PSR J2144−3933 with a period of 8.5 s (Young, Manchester & Johnston 1999), and the magnetar J1622−4950 (Levin et al. 2012), have modest modulation indices. Large modulation indices can also be found for younger short-period pulsars, especially when giant pulses are often observed (e.g. PSR J1047−6709 has $\bar{m} = 3.16 \pm 0.02$, caused by giant pulses as reported by Sun, Yan & Wang 2021). So it is evident that there is a large scatter of $\bar{m}$ on the reported evolution in the P–$\dot{P}$ diagram, reflected in the modest correlation coefficient.

Weltevrede et al. (2006) found no evidence for the modulation indices being affected by whether the subpulses are organized or not (whether there are drifting subpulses or not), but marginal evidence for pulsars with coherent drifting subpulses to have a lower modulation index. We find both $P_{\rm asym}$ and σ_{1/P_3} to be uncorrelated with $\bar{m}$ (see online material E). Also, no evidence is found for $\bar{m}$ being different for pulsars for which drifting subpulses or P_3-only features are detected (see online material E).

A reason for drifting subpulses to be more difficult to detect for less energetic pulsars could be the appearance of additional strong stochastic modulation, which would imply a higher modulation index. However, the different evolution of $\bar{m}$ and the probability of detecting drifting subpulses in the P–$\dot{P}$ diagram, as well as the non-correlation between $\bar{m}$ and drifting subpulses-related quantities, do not support this. Therefore, the main reason for drifting subpulses to be more prominent in some pulsars appears to be the stability of the produced subpulse patterns, rather than additional stochastic variability.

6 DISCUSSION

In this section, all the results related to subpulse modulation across the pulsar population are discussed. First this is done mathematically with minimum physical interpretation, progressing to a more explicit comparison to the carousel model.

6.1 Drifting subpulse population

As shown in Section 4, drifting subpulses are common and are detectable in about 60 per cent of the pulsars if sufficient S/N is available. This suggests that the physical conditions required for the drifting subpulse phenomenon cannot be distinctly different from those needed for the radio emission mechanism itself. However, some pulsars do not show drifting subpulses despite a high-S/N observation being available, suggesting that the non-detection is intrinsic to the pulsar. This could be caused by highly irregular drifting subpulse patterns, potentially amplified by aliasing, generating erratic changes in apparent drift direction. Furthermore, disruption of the drifting subpulse pattern by nulling and/or mode changing might cause pulsars only to show drifting subpulses for a fraction of the time.

Some pulsars that do not show drifting subpulses do exhibit other modulations, such as amplitude modulation (a P_3-only feature). In at least some pulsars, periodic amplitude modulation may well be linked to the same physical phenomenon as drifting subpulses, with the line of sight determining whether this manifests itself as subpulse drift or not.

We found that the observed P_3 distribution for pulsars with drifting subpulses shows V-shaped evolution such that at around $\tau_{\rm c} \simeq 10^{7.5}$ yr (or $\dot{E} \simeq 10^{31.5}$ erg s^{-1}), the smallest P_3 values are observed, and larger P_3 values are associated with both more and less energetic pulsars (Section 5.1). The minimum corresponds to $P_3 \simeq 2$, the Nyquist period. This strongly suggests that alias plays an important role. Aliasing is a sampling effect such that a beat between the rotation period and the intrinsic modulation period is observed. So a picture is emerging where the turning point in the P_3 distribution is interpreted as a change in alias order. The fact that at the high-$\dot{E}$ end of the distribution broader spectral features are observed (Section 5.2),

and the drifting subpulse features are less strong (Section 5.3), suggests a transition from high-$\dot{E}$ aliased modulation to unaliased lower $\dot{E}$ pulsars. This is further explored in Section 6.2.

Basu et al. (2019) report an anticorrelation between P_3 and $\dot{E}$ for pulsars with drifting subpulses, which they associate with low-$\dot{E}$ pulsars ($\dot{E} < 10^{32.5}$ erg s^{-1}). This anticorrelation is confirmed by the subset of our sample corresponding to a similar low $\dot{E}$ range below the turning point in the V-shaped evolution. However, our analysis of a larger sample suggests that the correlation is stronger in a P and $\dot{P}$ combination closer to τ_c than $\dot{E}$. Unlike for drifting subpulses, Basu et al. (2020) found periodic subpulse modulation in the form of amplitude modulation (modulation without evidence for phase drift) to occur throughout the full $\dot{E}$ range such that for $\dot{E} > 10^{32.5}$ erg s^{-1} it is the only form of periodic subpulse modulation.

They report that amplitude modulation typically has a $P_3 \sim$ 10–200, larger than those associated with drifting subpulses and uncorrelated with $\dot{E}$. We also concluded that P_3-only pulsars are seen in the full $\dot{E}$ range, and the mean P_3 for these pulsars is larger than that of drifting subpulses, and that no clear evolution of their P_3 values is seen across the P–$\dot{P}$ diagram (Section 5.1).

Basu et al. (2020) suggest that amplitude modulation forms a distinct class, with a different physical origin compared to drifting subpulses. It can be noted that other pulsar properties also show a transition at a comparable $\dot{E}$, such as profile morphology (e.g. Rankin 2022) and linear polarization (e.g. Weltevrede & Johnston 2008; Posselt et al. 2022). However, our sample includes pulsars above $\dot{E} > 10^{32.5}$ erg s^{-1} for which clear drifting subpulses are identified (examples include PSRs J1453−6413, J1645−0317, and J1918+1444). This suggests that there is no sharp transition between pulsars with drifting subpulses and those with amplitude modulations. This conclusion is further strengthened by the fact that the evolution of the drift rate is gradual, such that high-$\dot{E}$ pulsars show less strong pulse phase modulation (see Fig. 9). The larger drift rate at high $\dot{E}$ could be interpreted to mean either that there is more additional erratic emission biasing the P_2 measurements, or an actual evolution in drift rate. In any case, this strongly suggests that many pulsars in the P_3-only class will have weak subpulse phase modulation that is hard to detect. However, this does not explain the fact that P_3-only pulsars have typically larger P_3 values, suggesting that for some P_3-only pulsars the modulation is governed by different physics. For example, some of the P_3-only features may be caused by periodic nulling.

6.2 Modelling the P_3 evolution

In Section 6.1, it was demonstrated that the distribution of the observed P_3 is V-shaped. We consider the direction of evolution of P_3 in the P–$\dot{P}$ diagram as found in Section 5.1, i.e. $a/b = -1.7$. Hereafter, we use symbol $\xi = (P/\mathrm{s})^{-1.7}(\dot{P}/10^{-15})$ to describe the P_3 evolution, and in effect regard it as a proxy both for the characteristic and the true age of the pulsar. The observed evolution is shown in Fig. 12 with blue points, and is characterized by large P_3 values for low and high ξ, and the smallest P_3 values dominate the region with $\xi \sim 0.8$. The fact that the turning point of the distribution occurs at $P_3 \sim 2$ strongly suggests a transition between (first-order) aliased and non-aliased subpulse modulation. Furthermore, in this interpretation, the non-aliased drift in older pulsars is suggested by drifting subpulses being stronger and more stable (larger P_{asym} and smaller σ_{1/P_3}) compared with those of younger pulsars. The purpose of this section is to demonstrate that it is possible to find a monotonic relationship between P_3^{int}, the intrinsic P_3, and ξ that can plausibly reproduce both the unaliased and aliased observed values of P_3. This will be done without considering a specific physical origin for the drifting subpulses.

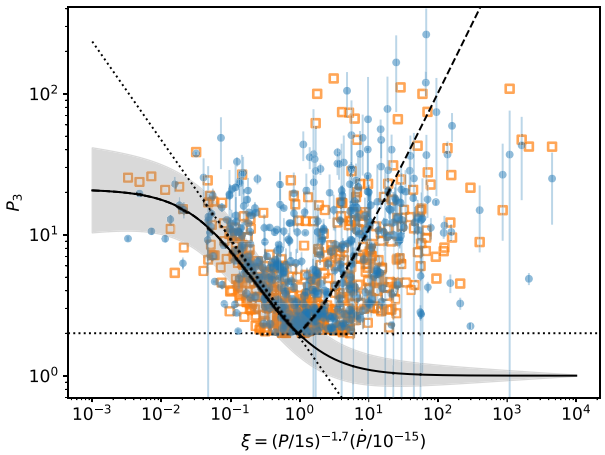

Figure 12. A comparison between the observed P_3 values (blue points) with a simulation (orange open squares) as a function of ξ (the P–$\dot{P}$ combination for which P_3 is observed to evolve strongest). The simulation assumes that the intrinsic P_3 decreases with ξ (solid line). When the intrinsic $P_3 < 2$ (horizontal dotted line), the observed P_3 will be aliased. The dashed line (equation 8) is the aliased version of the solid line. Intrinsic P_3 values are drawn at random from the model, where the grey shaded region indicates the width of the distribution. The intrinsic P_3 values are transformed to the observed P_3 after taking alias into account (equation 7). The diagonal dotted line represents a power-law relationship with an exponent equal to −0.7.

To test if a model where the intrinsic P_3 monotonically decreases with ξ can reproduce the data, a synthetic sample of pulsars is generated by considering a description of $P_3^{\mathrm{int}}(\xi)$. When $P_3^{\mathrm{int}} < 2$, alias occurs and we take its lowest order aliased value (see e.g. Edwards & Stappers 2002)

$$\frac{1}{P_3} = \left| \frac{1}{P_3^{\mathrm{int}}} - 1 \right|. \tag{7}$$

Note that this approach is independent of any physical model, as it is a mathematical description of alias and it relies only on the fact that the emission is observed once per stellar rotation.

We first considered $P_3^{\mathrm{int}}(\xi)$ to follow the diagonal dotted line in Fig. 12. By design, this would describe the data in the low-ξ (typically older pulsars) region well. At high ξ (younger pulsars), high alias orders (not included in equation 7) are implied by the $1/P_3^{\mathrm{int}} \gg 0.5$ (very fast modulation) reached. As a consequence, the model fails to reproduce the systematic increase of the observed P_3 for $\xi \gtrsim 0.8$ because a near-uniform distribution in apparent P_3 would be expected. To avoid this, we insist on a model where the alias order remains small, such that either an unaliased P_3 is observed, or the lowest possible order alias described by equation (7). This requires a relation for $P_3^{\mathrm{int}}(\xi)$ that flattens out at large ξ compared to the diagonal dotted line in Fig. 12.

The dashed line in Fig. 12 represents the aliased P_3 observed at large ξ. This line reproduces the observed increase of P_3 with ξ, and we define this line as

$$P_3(\xi) = (\xi - q)^k / w. \tag{8}$$

The unaliased P_3^{int} (obtained with equation 7), extended over the full ξ range, is represented as the solid line. The specific choice of $q = -1.05$, $w = 1$, $k = 1$ is used. These parameters ensure that the Nyquist point ($\xi = q + 2w$) is close to 1, and that $P_3(\xi)$ flattens at low ξ ($q + w < 0$). Other functional forms may fit the data equally

well, but it is important to realize that, however contrived the relation between the dashed and solid curves appears in a P_3 plot, the chosen forms are simply related via equation (7).

Overall, the solid line in Fig. 12 represents a monotonic gradual increase of the intrinsic modulation period as the pulsar ages (evolves towards lower ξ). If interpreted as a carousel of beamlets, this would be an evolution from being initially fast circulation relative to the neutron star surface to near stationary as the pulsar 'dies'. Young pulsars are then observed to have a large single-aliased P_3 given by the dashed line. It should also be noted that since the dashed and solid lines are aliases of each other, a monotonic increasing and decreasing $P_3^{\rm int}(\xi)$ could explain the observed P_3 evolution equally well, although we have argued in Section 6.1 that an increasing $P_3^{\rm int}$ with $\tau_{\rm c}$ is preferred by the observations.

The model for P_3 (solid line for small ξ, dashed line for large ξ) fits the observed distribution well (blue points). Fig. 12 also shows the consequence of allowing a moderate degree of scatter (grey shaded region) around the underlying model for $P_3^{\rm int}$ (solid line). The synthetically generated orange squares are drawn from this distribution, and transformed to the observed P_3. The distribution of orange squares matches that of the blue points well, including the observed scatter, thereby demonstrating that the observed non-monotonic evolution of P_3 can be reproduced with a monotonic evolution of $P_3^{\rm int}$.

In the model, it is assumed that the fractional uncertainty in $P_3^{\rm int}$ decreases from 0.5 at $\xi = 10^{-3}$ to 0.01 at $\xi = 10^{4}$. This indicates that the increased scatter in observed P_3 values for young (high ξ) pulsars is a consequence of aliasing boosting the scatter in $P_3^{\rm int}$, while according to the model $P_3^{\rm int}$ is better defined for these pulsars. This boost of variability in $P_3^{\rm int}$ is argued in Section 5.2 to be responsible for the evolution in spectral width as well. A reason for an increased scatter in $P_3^{\rm int}$ for older pulsars is the observation that drift mode changes are more likely for these pulsars (see Section 5.1).

6.3 P_2 evolution

So far, the results have been discussed independent of a specific model for drifting subpulses. Here, some geometric effects are discussed in the context of the rotating carousel model where the drifting subpulses are produced by a number of subbeams rotating around the magnetic axis.

It was found that pulsars with a higher $\dot{E}$ tend to have larger P_2 (Section 5.4). Two possible interpretations were suggested. It could relate to an increased stochastic subpulse modulation, which skews the measured P_2. Alternatively, it can geometrically be interpreted as a reduction of the number of beamlets in the carousel. Here, we discuss implications of the latter interpretation. However, additional geometric effects related to this interpretation will be considered first.

The evolution in pulse width W is expected to contribute to the P_2 evolution. A larger W means that the subbeams can be expected to be further separated in pulse longitude, and for typical geometries $P_2 \propto W$. Pulsars with larger $\dot{E}$ tend to have larger W (e.g. Johnston & Karastergiou 2019; Posselt et al. 2021). Therefore, from this effect, one would expect that P_2 is larger for high-$\dot{E}$ pulsars. One factor affecting the W evolution is the evolution of the magnetic inclination angle α, which is aligning over the lifetime of a pulsar (e.g. Lyne & Manchester 1988; Tauris & Manchester 1998; Weltevrede & Johnston 2008; Johnston & Karastergiou 2017). However, alignment would predict W to typically be larger for older pulsars, opposite to what is observed (e.g. Johnston & Karastergiou 2019; Posselt et al. 2021). This suggests that other factors (especially the shrinking of the polar cap over time) dominate the observed increase of W towards high-$\dot{E}$ pulsars. Nevertheless, to test whether our conclusions related to P_2 evolution are affected by W evolution, the evolution of P_2/W_{50} is assessed (see Appendix C). This shows that also P_2/W_{50} tends to be higher for high-$\dot{E}$ pulsars; hence, the conclusion that they tend to have a smaller number of subbeams remains valid.

P_2 is related to the so-called complexity parameter (e.g. Gil & Sendyk 2000), defined as $C = 2r_{\rm p}/\Delta$, where $2r_{\rm p}$ is the polar cap diameter and Δ is the typical separation between beamlets. The pulse width relates to $2r_{\rm p}$ for a central line-of-sight cut. Therefore, for a packed polar cap with subbeams, C represents the number of subbeams crossed by the line of sight, hence relates to the expected complexity in the pulse structure. Since Δ would correspond to P_2 in pulse longitude, C can also be expressed as W/P_2 for a central cut. More generally, one can expect $C \propto (P_2/W)^{-1}$. As discussed, pulsars with a larger $\dot{E}$ tend to have a larger P_2/W; hence, C can be expected to be small.

Observationally, C has been linked to modulation indices, which measure the amount of variability of single pulses. Jenet & Gil (2003) argue that a high C implies overlapping subpulses, hence a reduced modulation index. Therefore, $\bar{m}$ and C are thought to be anticorrelated. In Section 5.6, it was found that large-P pulsars typically have a larger $\bar{m}$. This should correspond to a small C, hence a large P_2/W. However, large P_2/W are found to associate to larger $\dot{E}$ pulsars that tend to have small P. This suggests that the evolution of $\bar{m}$ is governed by more than C, such as an evolution in the variability of the individual subbeams.

Specific physical models for subpulse generation can predict the scaling of C with P and $\dot{P}$ (Jenet & Gil 2003). These include the Ruderman & Sutherland (1975) sparking gap model (see also Gil & Sendyk 2000), and three other models, which relate to continuous current outflow instabilities (Arons & Scharlemann 1979; Hibschman & Arons 2001), surface magnetohydrodynamic wave instabilities (Lou 2001), and outer magnetospheric instabilities (Jenet & Gil 2003). However, none of the P and $\dot{P}$ dependence of these four predictions for C (see Jenet & Gil 2003) correlates with the found evolution of $\bar{m}$ with P and $\dot{P}$. A linear fit of equation (5) reveals that $b/a = 0.11 \pm 0.07$, inconsistent with the predicted b/a of $-4/9$, $-1/3$, 1, and $-1/5$, respectively. This again might suggest that the physics governing C is not directly related to $\bar{m}$, rather than that the models for C are incorrect.

6.4 Comparison with theoretical models

We demonstrated in Section 6.2 that the origin for the apparent V-shaped P_3 evolution is suggestive of aliasing. The model employed (equation 8) is purely mathematical, without imposing specific physics to the drifting subpulse phenomenon. Here, we discuss the results in light of the geometric and physical notions of emission carousels and $\boldsymbol{E} \times \boldsymbol{B}$ drift, concepts first introduced by Ruderman & Sutherland (1975) (hereafter RS) and since developed by many authors (e.g. Gil & Sendyk 2003).

A prediction of the carousel model is that the measured P_3 is determined by the circulation time of the carousel and the number of subbeams within the polar cap. As a consequence, in general different profile components should have identical P_3 values. Fig. 13 shows a scatter plot for pulsars for which relatively well defined P_3 values are measured in separate pulse profile components. A tight correlation is observed, with most pulsars having consistent P_3 values for different components. Some exceptions exist (PSRs J1224−6407, J1345−6115, J1427−4158, J1430−6623, and J1722−3207 in the figure). Exceptions are to be expected in the presence of drift

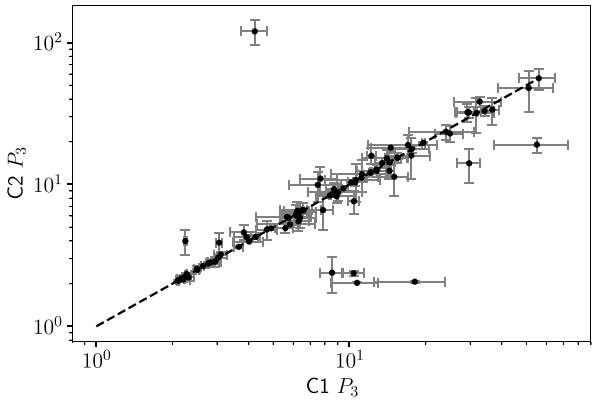

Figure 13. Comparison of P_3 values as measured in two profile components of the same pulsar. For clarity, only relatively well defined spectral features with $P_3 < 3\sigma_{1/P_3}$ are shown. The dashed line corresponds to equal P_3 values for the two components.

mode changes (see also Section 5.1). In addition, so-called core components can have separate modulations. The correlation therefore powerfully demonstrates that drifting subpulse patterns in separate profile components are linked to a single physical origin, as is expected in a carousel.

Accepting that carousels are present on or just above polar caps (whose minimum size is defined by the last open fieldline touching the light cylinder), it is commonly assumed that their drift over the surface, so-called $\boldsymbol{E} \times \boldsymbol{B}$ drift, directly reflects a particle flow and emission on the open fieldlines.

Although exceptional circumstances may apply in specific pulsars, the general nature of $\boldsymbol{E} \times \boldsymbol{B}$ drift is to be weak (i.e. near-corotation) in young fast pulsars and speed up rapidly as a pulsar ages and spins down (being dependent on the acceleration parameter $\sim B/P^2$). This is true both in its original formulation in RS and later modifications (Gil et al. 2003). Such behaviour is exactly the opposite of what our observations suggest.

It can be pointed out that we do not directly observe the circulation time, but P_3, which depends on the number of sparks in the carousel. However, to reproduce the observed P_3 evolution, the spark number would have to increase dramatically when applied to younger pulsars – and again our measurements show that if the number of sparks changes, it is in exactly the opposite sense (Section 6.3). Thus, $\boldsymbol{E} \times \boldsymbol{B}$ physics cannot plausibly yield the solid line of Fig. 12, which we argue represents the intrinsic subpulse drift.

We therefore face a paradox. Drift explained by the acceleration parameter would result in values of the circulation time (and hence of P_3 for any likely number of sparks) that decreases as the pulsar ages from right to left in Fig. 12. In fact, such measured values do appear in the figure, but we have interpreted them as lowest order aliased with their true values close to $P_3 \sim 1$.

One way out would be to suppose that the left and right halves of Fig. 12 are governed by different physics (Basu et al. 2016, 2020), an assumption weakened by our results (Section 6.1). In any case, such a model would mean that by coincidence the transition at $P_3 \sim 2$ has both a physical significance and plays its role as an alias boundary dependent on our sampling rate P. An important feature of our results is the continuity of the drift phenomenon throughout pulsar evolution.

Alternatively, we can abandon the assumption that the solid black curve in Fig. 12 represents direct observation of $\boldsymbol{E} \times \boldsymbol{B}$-driven drift, while still insisting that it describes observations of real spark motion. However, this line is mathematically related to the dashed alias line – and it is the dashed line that is approximately consistent with the magnitude and variation of RS-predicted $\boldsymbol{E} \times \boldsymbol{B}$ drift. As stressed earlier, each line is the alias of the other. The P_3 system we observe can therefore be seen as our periodic sampling of the beat between an internal $\boldsymbol{E} \times \boldsymbol{B}$ system within the pulsar and the pulsar period itself (see Wright 2022).

One advantage of this interpretation is that the apparent drift reversals found in some older pulsars (e.g. J1750−3035; Szary et al. 2022) can naturally be understood as a slight variation in $\boldsymbol{E} \times \boldsymbol{B}$ without appeal to observational aliasing, and the pulsar's $\boldsymbol{E} \times \boldsymbol{B}$ does not change sign. Sudden changes in drift rates can also be seen as loss or gain of a subbeam in a near-fixed $\boldsymbol{E} \times \boldsymbol{B}$ environment. These and related points are further discussed in Wright (2022).

A particularly interesting feature of this approach (to be pursued in more detail elsewhere) is the formulation of the expected observable P_3 represented by the dashed line in Fig. 12. This now can be seen as representing the underlying $\boldsymbol{E} \times \boldsymbol{B}$ system of the pulsar that our periodic sampling reveals. It is now possible to apply the acceleration parameter to pulsars on this line and estimate the spacing and number of polar cap sparks within the pulsars' beat system. If the polar cap has a radius $r_\mathrm{p} \propto s/P^{1/2}$ so that the N sparks have a separation $\Delta \approx 2\pi r_\mathrm{p}/N$, then it can be shown that

$$P_3 \simeq s \left(\frac{\Delta}{95\ \mathrm{m}}\right) \left(\frac{P\dot{E}}{3 \times 10^{31}\ \mathrm{erg}}\right)^{\frac{1}{2}}, \tag{9}$$

where P_3 represents the values on the dashed alias line [see equation (9) of Wright 2022], and s is the ratio of the actual r_p to that defined by the last closed field line touching the light cylinder. Divergences from the line $P_3 \propto (P\dot{E})^{1/2}$ are a measure of the product $s \times \Delta$. The significance here is that the dependence of P_3 on $P\dot{E}$ in equation (9) is derived on a purely theoretical basis and implies $a/b = -2$, a near-coincidence with the observationally derived result of Section 5.1 ($a/b = -1.7 \pm 0.3$), and would imply a value $k = 1/2$ in equation (8). Application of this equation both to pulsars individually and collectively could give realistic estimates of $s \times \Delta$ to be compared with profile and polarization data.

7 CONCLUSIONS

A catalogue of subpulse modulation properties at 1280 MHz is presented, reporting on the findings of a systematic analysis of the subpulse modulations for 1198 pulsars in the TPA single-pulse legacy data. The wealth of single-pulse data, with 1.6 million pulses analysed and covering a significant fraction of the known pulsars, allows a detailed investigation into the evolution of various drifting subpulse-related quantities across the pulsar population. By design, the obtained data set is suitable with sufficient quality and length to identify drifting subpulses in many sources. A semi-automated process and new techniques are developed, with shuffle-normalized spectra aiding identification of weak (possibly broad) spectral features and the assessment of their significance. In the course of the analysis, we corrected the periods and spin-down rates for 12 pulsars, for which harmonically related values were reported in the literature.

The strength of subpulse modulation across the population of pulsars is quantified with a flux density-weighted and pulse longitude-averaged modulation index $\bar{m}$. Our results reveal that $\bar{m}$ evolves most strongly with P such that large-P pulsars tend to have larger $\bar{m}$. Although $\bar{m}$ evolution has been linked to the evolution of a 'complexity parameter' in the past, our observations suggest that it

is not the dominant relevant physical parameter. Instead, the intrinsic variability of subbeams might play a more important role.

Although the focus of this paper is drifting subpulses, we also identify a class of pulsars where amplitude modulations with a period P_3 are found but without subpulse phase modulations (so-called P_3-only pulsars). These are found to be distributed roughly uniformly throughout the pulsar population. Some modulations of this nature may be generated by nulling or mode changing. However, there is no evidence of a sharp transition between such pulsars and those with drifting subpulses. This therefore strongly suggests that many P_3-only pulsars have weak drift that is hard to detect.

Drifting subpulses are detected across a wide range of the P–$\dot{P}$ space. For 35 per cent of pulsars in our sample (418 in total) drifting subpulses are identified. This implies that 60 per cent of the overall population of pulsars would be found to have detectable drifting subpulses if data with sufficient S/N were available. Unlike the P_3-only pulsars, drifting subpulses are more likely to be detected for the older and less energetic pulsar population, and their P_3 values are typically smaller.

The modulation periods P_3 for pulsars with drifting subpulses are found to follow a V-shaped evolution in the P–$\dot{P}$ diagram such that at a characteristic age $\tau_c \simeq 10^{7.5}$ yr the smallest P_3 values are observed. Both older and younger pulsars typically have larger P_3, with the minimum occurring at the Nyquist period $P_3 \simeq 2$. This strongly points to alias being a fundamental ingredient required for the understanding of drifting subpulse evolution. The V-shaped evolution of P_3 can be reproduced, in a way that is independent of a specific physical model, by a monotonically evolving intrinsic underlying $P_3^{\rm int}$. In this interpretation, pulsars evolve from a fast $P_3^{\rm int}$ with observed aliased $P_3 > P_3^{\rm int}$ (typically of the lowest order for pulsars with small τ_c) to unaliased $P_3 = P_3^{\rm int}$ (for pulsars with large τ_c).

This mathematical description of drifting subpulses offers an explanation for various observed trends. The small-τ_c (large-$\dot{E}$) pulsars are naturally expected to have more erratic subpulse modulation patterns because the alias effect will enhance the observed effect of any irregularities in the underlying subpulse modulation. So this interpretation not only describes the observed P_3 evolution, but also explains why drifting subpulses are more often detected in large-τ_c pulsars. Furthermore, for small-τ_c pulsars with drifting subpulses, it explains their broader (less well defined P_3) and weaker (less systematic drift) spectral features, and their more erratic drifting subpulse patterns may generate bias in the observed evolution of P_2.

A natural geometric representation of drifting subpulses is to see them modelled as a carousel of discrete subbeams rotating around the magnetic axis. Since we find evidence that the number of subbeams does not decrease for larger τ_c, our interpretation of the observed P_3 implies that the carousel must slow down as it evolves with $P_3^{\rm int}$ increasing.

This creates an apparent contradiction to the conventional view that carousel rotation is driven by the $\boldsymbol{E} \times \boldsymbol{B}$ effect. Measured by the original RS formula, the carousel drift should begin as near-corotation and gradually accelerate as a pulsar ages. Here, we find exactly the opposite. Later changes introduced by partial screening of the polar cap potential (e.g. Gil et al. 2003; Basu et al. 2016) have successfully modified this view. However, this model in its present form cannot be extended to young pulsars.

To resolve this, we suggest that the observed subpulse modulation represents a sampling of a beat system, internal to the pulsar, between its $\boldsymbol{E} \times \boldsymbol{B}$ time-scale and its rotation period (Wright 2022). The polar carousel of subbeams is then seen as generated by time-delayed interaction between separate regions of the magnetosphere. Such a carousel would initially drift strongly relative to the neutron star and gradually slow as the pulsar ages, which is what our observations suggest.

ACKNOWLEDGEMENTS

The MeerKAT telescope is operated by the South African Radio Astronomy Observatory, which is a facility of the National Research Foundation, an agency of the Department of Science and Innovation. Pulsar research at Jodrell Bank Centre for Astrophysics and Jodrell Bank Observatory is supported by a consolidated grant from the UK Science and Technology Facilities Council (STFC). XS acknowledges financial support from the President's Doctoral Scholar Award. GW thanks the University of Manchester for Visitor status. MeerTime data are housed and processed on the OzSTAR supercomputer at Swinburne University of Technology. MB acknowledges support from ARC grant CE170100004.

DATA AVAILABILITY

The data underlying this article will be shared on reasonable request to the corresponding author. See also Appendix A.

REFERENCES

Arons J., Scharlemann E. T., 1979, ApJ, 231, 854
Ashworth M., 1982, PhD thesis, Victoria Univ. Manchester, UK
Backer D. C., 1970, Nature, 227, 692
Backus P. R., 1981, PhD thesis, Univ. Massachusetts Syst.
Bailes M. et al., 2020, Publ. Astron. Soc. Aust., 37, e028
Basu R., Mitra D., Melikidze G. I., Maciesiak K., Skrzypczak A., Szary A., 2016, ApJ, 833, 29
Basu R., Mitra D., Melikidze G. I., Skrzypczak A., 2019, MNRAS, 482, 3757
Basu R., Mitra D., Melikidze G. I., 2020, ApJ, 889, 133
Biggs J. D., McCulloch P. M., Hamilton P. A., Manchester R. N., Lyne A. G., 1985, MNRAS, 215, 281
Caleb M. et al., 2022, Nat. Astron., 6, 828
Champion D. J. et al., 2005, MNRAS, 363, 929
Deshpande A. A., Rankin J. M., 1999, ApJ, 524, 1008
Deshpande A. A., Rankin J. M., 2001, MNRAS, 322, 438
Drake F. D., Craft H. D., 1968, Nature, 220, 231
Edwards R. T., Stappers B. W., 2002, A&A, 393, 733
Gil J. A., Sendyk M., 2000, ApJ, 541, 351
Gil J. A., Sendyk M., 2003, ApJ, 585, 453
Gil J., Melikidze G. I., Geppert U., 2003, A&A, 407, 315
Gogoberidze G., Machabeli G. Z., Melrose D. B., Luo Q., 2005, MNRAS, 360, 669
Gupta Y., Gil J., Kijak J., Sendyk M., 2004, A&A, 426, 229
Hibschman J. A., Arons J., 2001, ApJ, 560, 871
Hotan A. W., van Straten W., Manchester R. N., 2004, Publ. Astron. Soc. Aust., 21, 302
Huguenin G. R., Taylor J. H., Troland T. H., 1970, ApJ, 162, 727
Jenet F. A., Gil J., 2003, ApJ, 596, L215
Johnston S. et al., 2020, MNRAS, 493, 3608
Johnston S., Karastergiou A., 2017, MNRAS, 467, 3493
Johnston S., Karastergiou A., 2019, MNRAS, 485, 640
Kou F. F. et al., 2021, ApJ, 909, 170
Levin L. et al., 2012, MNRAS, 422, 2489
Levin L. et al., 2019, MNRAS, 488, 5251
Lou Y.-Q., 2001, ApJ, 563, L147
Lyne A. G., Manchester R. N., 1988, MNRAS, 234, 477
Manchester R. N., Hobbs G. B., Teoh A., Hobbs M., 2005, AJ, 129, 1993
Nowakowski L. A., 1991, ApJ, 377, 581
Oswald L. S. et al., 2021, MNRAS, 504, 1115
Posselt B. et al., 2021, MNRAS, 508, 4249
Posselt B. et al., 2023, MNRAS, 520, 4582

Qiao G. J., Lee K. J., Zhang B., Xu R. X., Wang H. G., 2004, ApJ, 616, L127
Rankin J. M., 1986, ApJ, 301, 901
Rankin J., 2022, MNRAS, 514, 3202
Rosen R., Clemens J. C., 2008, ApJ, 680, 671
Ruderman M. A., Sutherland P. G., 1975, ApJ, 196, 51 (RS)
Serylak M. et al., 2009, MNRAS, 394, 295
Song X. et al., 2021, MNRAS, 505, 4456
Song X. et al., 2023, The Thousand-Pulsar-Array programme on MeerKAT – VIII. The subpulse modulation of 1198 pulsars (1.0) [Data set]. Zenodo. Available at: https://doi.org/10.5281/zenodo.6900582.
Sun S. N., Yan W. M., Wang N., 2021, MNRAS, 501, 3900
Szary A., van Leeuwen J., 2017, ApJ, 845, 95
Szary A., van Leeuwen J., Wright G., Weltevrede P., Agar C. H., Tiburzi C., Maan Y., Keith M. J., 2022, ApJ, 934, 23
Tan C. M. et al., 2018, ApJ, 866, 54
Tauris T. M., Manchester R. N., 1998, MNRAS, 298, 625
Taylor J. H., Huguenin G. R., 1971, ApJ, 167, 273
van Straten W., Bailes M., 2011, Publ. Astron. Soc. Aust., 28, 1
Wang N., Manchester R. N., Johnston S., 2007, MNRAS, 377, 1383
Weltevrede P., 2016, A&A, 590, A109
Weltevrede P., Johnston S., 2008, MNRAS, 391, 1210
Weltevrede P., Edwards R. T., Stappers B. W., 2006, A&A, 445, 243
Weltevrede P., Stappers B. W., Edwards R. T., 2007, A&A, 469, 607
Wolszczan A., 1980, A&A, 86, 7
Wright G., 2022, MNRAS, 514, 4046
Wright G., Weltevrede P., 2017, MNRAS, 464, 2597
Young M. D., Manchester R. N., Johnston S., 1999, Nature, 400, 848
Zhang B., Harding A. K., Muslimov A. G., 2000, ApJ, 531, L135

SUPPORTING INFORMATION

Supplementary data are available at *MNRAS* online.

Table 2. A summary of the spectral subpulse modulation measurements.
Table A1. A summary of observation related parameters.
Appendix D. Further description of the subpulse modulation analysis and the sample.
Appendix E. Supplementary population analysis.

Please note: Oxford University Press is not responsible for the content or functionality of any supporting materials supplied by the authors. Any queries (other than missing material) should be directed to the corresponding author for the article.

APPENDIX A: ONLINE TABLES AND FIGURES

The full Table 2 and all original and shuffle-normalized spectra can be found here.[8] In the same place, Table A1 can be found, which contains additional information related to the observations. Both tables can also be found in the supplementary material associated with this publication.

APPENDIX B: SPECTRAL ANALYSIS

The on-pulse regions are algorithmically defined as that part of the template where the amplitude exceeds 1 per cent of the maximum amplitude. This either forms a single interval that is labelled as the MP, or an MP and an IP interval if the amplitude of the template is below 1 per cent roughly in between the MP and IP. In this work, that part of the profile where the maximum amplitude of the template occurs is labelled as the MP. In some cases, the analysis benefits from splitting the profile into at most two components. Unless the components are defined manually, the split is applied at the first minimum following the first (possibly local) maximum amplitude in the template in the relevant on-pulse region. Further details about the MP/IP definition and profile splitting can be found in the online material D2.

The FFT length used for the spectra is at most 512 pulses (or the largest power of two that fits in the length of the pulse sequence), and the minimum is limited to 64 pulses. The number of pulses that contributes to the LRFS is a multiple of the FFT length, so reducing the FFT length could lead to the inclusion of more pulses in the analysis. In addition, a lower spectral resolution is preferred if the S/N is relatively low. The FFT length used for the calculation of the longitude-resolved modulation index is always 16 pulses since spectral resolution is not required, and short FFT lengths are preferred as it ensures most pulses can be used in the analysis. See online material D5 for further details.

The dynamic range used for the colour range for the LRFS (see e.g. colour bar on the right of panel a ii) of Fig. 1) is such that 98 per cent of the spectral values in the pulse longitude range shown occupy at least 50 per cent of the dynamic range. This could require clipping to be applied: samples exceeding a threshold value corresponding to the darkest colour are set to the threshold. The level of clipping applied can be read from the numerical scale next to the colour scale. If the maximum value is less than that indicated with 'Max.' next to this, clipping has been applied. So in the case of the LRFS for PSR J1539−6322 in panel (a ii) of Fig. 1, the largest spectral sample is about 1.00/0.02 = 50 times stronger than the colour scale suggested. This helps to emphasize the weaker spectral features, such as in this case the first harmonic.

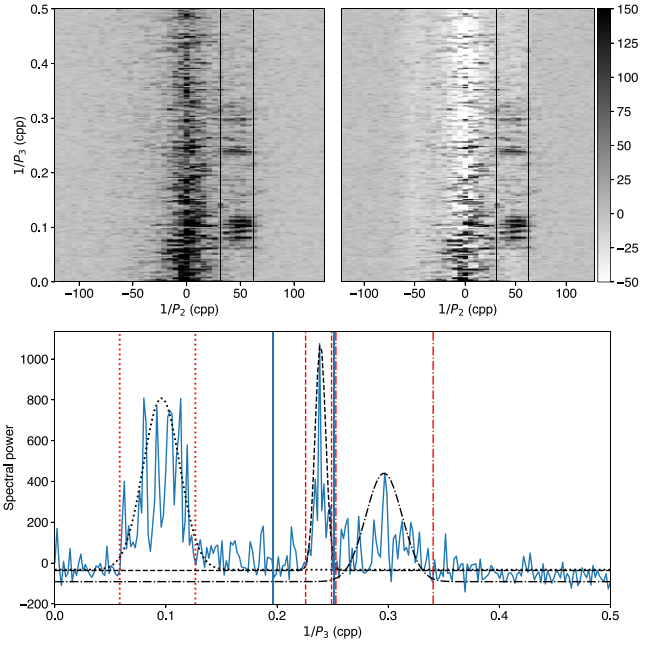

Figure B1. The top left and right panels show, respectively, the original and shuffle-subtracted 2DFS for PSR J0108−1431. The bottom panel shows the 2DFS power integrated between the vertical solid lines as shown in the top panels. There are three spectral features, covering the ranges indicated with dotted, dashed, and dash–dotted lines. The three Gaussians are defined by the determined μ_{1/P_3} and σ_{1/P_3}, with a baseline/amplitude corresponding to the lowest/largest spectral power within the $1/P_3$ range covering the feature.

[8] 10.5281/zenodo.6900582

As for the LRFSs, the dynamic range of the 2DFSs is adjusted to ensure that weak features are visible by clipping the brightest features. The applied algorithm is identical to that used in the LRFS. Only samples in the shown $1/P_2$ range are considered, and either the full $1/P_3$ range or that highlighted by the dotted lines in the 2DFS is used. All spectral powers are normalized in the produced plots.

For the 2DFS, the full available $1/P_2$ range is not always shown, since the spectral power tends to be concentrated towards $1/P_2 = 0$. The shown range is algorithmically determined by ensuring that at least 90 per cent of the spectral power is shown. The shown range is always symmetric with respect to $1/P_2 = 0$, and no fewer than two spectral bins at either side of the shown range are excluded when the full range is not shown. In 57 cases, the shown range is defined manually to ensure that all defined features are fully visible. The $1/P_2$ ranges of the shuffle-normalized 2DFSs always match those of the regular 2DFSs for easier comparison.

The shuffle-normalized spectra suppress the stochastic pulse-to-pulse variability, which often manifests itself as a vertical band of excess power in the middle of the 2DFS. However, it can be reduced too much resulting in negative powers to appear. This is most noticeable in the shuffle-normalized LRFS (panel d ii of Fig. 1) that has distinctly negative spectral power away from the ∼0.08 cpp feature. This is because the shuffling process randomizes (smears out in the $1/P_3$ direction) all variability, including the power associated with the organized drifting subpulses. So the average spectral power that gets subtracted will overestimate the spectral power associated with stochastic pulse-to-pulse variability. Despite this artefact, the shuffle-normalized spectra have proven to be an effective tool to identify weak spectral features of interest.

The vertically integrated power of the visually most dominant drifting subpulse feature, otherwise the clearest P_3-only feature, is shown in the bottom panel of the 2DFS. The approximate range in $1/P_3$ occupied by the feature is indicated by the two horizontal lines in the 2DFS. In the case of column (e) in Fig. 1, this implies that the weaker drift feature is shown in the bottom panel attached to the 2DFS. The spectral feature in the bottom panel always corresponds to the orange feature in the left side panel of the 2DFS. The dotted lines are also shown in the left side panel of the 2DFS. The thicker dotted lines indicate the feature that is visually dominant when there are multiple profile components with spectral features. So in the case of PSR J1539−6332 in column (a) of Fig. 1, the dominant feature is the one in the first 2DFS. The dominant feature is used in the statistical analysis when spectral properties of different pulsars are compared.

To assess the significance of the spectral features, a number of diagnostics are utilized. The pulse sequence is split into two shorter sequences with half the number of pulses to verify that the feature is persistent. Where multiple observations of the same pulsar are available, these could similarly be used. The shuffle-normalized plots provide a quick indication of the significance of features in the presence of stochastic pulse-shape variability. Following Weltevrede et al. (2006, 2007), the P_3 and P_2 of the identified spectral features are measured by determining the centroid of the spectral power within rectangular regions in the 2DFS. An error on the centroid follows from the rms determined from the off-pulse spectra. However, in most cases the systematic error arising from the subjectivity in the selection of the rectangular region dominates the uncertainty. To quantify this, multiple somewhat different rectangular regions are considered. The quoted errors correspond to the range of centroid locations (and their errors). In order for a feature to be classed as a drifting subpulse feature, the sign of the derived P_2 should be constrained within the quoted error.

Unlike P_3, P_2 depends on observing frequency as well as pulse longitude (e.g. Weltevrede et al. 2006, 2007). This makes P_2 a somewhat ill-defined quantity. An additional complication in measuring P_2 from the 2DFS is that in general there is stochastic pulse-shape variability leading to power concentrated along the vertical axis. This introduces a bias in P_2 such that it is measured to be further away from zero than the actual P_2 corresponding to the drifting subpulses. This bias also makes the error on P_2 asymmetric; hence, separate errors in both directions are quoted. The 2DFS of PSR J1539−4828 (panel b iii of Fig. 1) shows that changes in the alias order are another reason for the determined centroid of a spectral feature to deviate from what corresponds to the typical subpulse separation P_2.

The spectral width σ_{1/P_3} is determined using an approach similar to that used to produce the shuffle-normalized spectra (see Section 2.3.4). An example of the shuffle-subtracted 2DFS for PSR J0108−1431 is shown in the top right panel of Fig. B1, with the original spectrum showing in top left and the resulting integrated spectral power in the bottom panel. As discussed in the context of the shuffle-normalized spectra, the baseline subtraction can overcompensate, resulting in negative spectral powers. To avoid this affecting the measurement of the spectral widths, the baseline is raised such that no negative spectral powers are left in the integrated spectrum within the $1/P_3$ range covered by the spectral feature.

The spectrum in Fig. B1 has three drift modes identified as indicated by the vertical lines in the bottom panel. The three Gaussian curves show the derived μ_{1/P_3} and σ_{1/P_3}, as well as the applied baseline that is different for the three features. The calculated σ_{1/P_3} represents the widths of the spectral features well.

APPENDIX C: ADDITIONAL POPULATION ANALYSIS

Fig. C1 shows the distribution of P_3 in the P–$\dot{P}$ diagram for pulsars with their dominant spectral feature being P_3-only. Unlike Fig. 3 (for pulsars for which the dominant spectral feature is associated

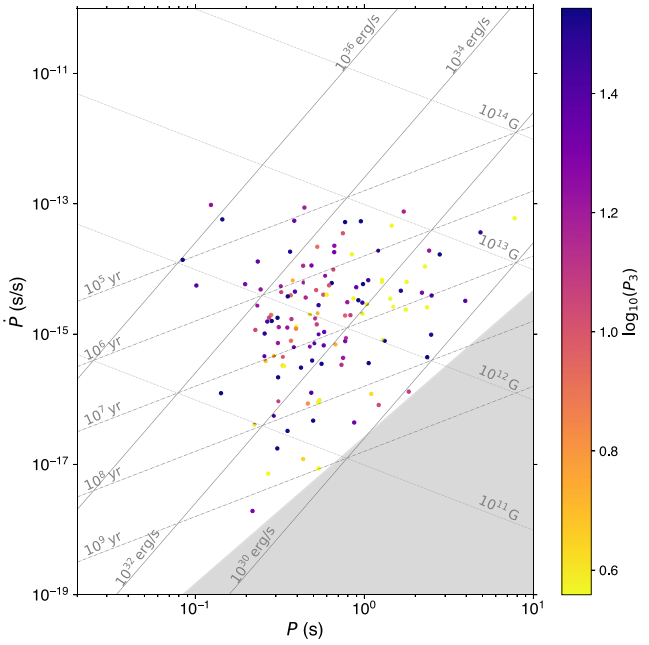

Figure C1. P–$\dot{P}$ diagram where the colours of the dots represent $\log_{10}(P_3)$ for each pulsar with a dominant P_3-only spectral feature. See the caption of Fig. 3 for a description of the various lines.

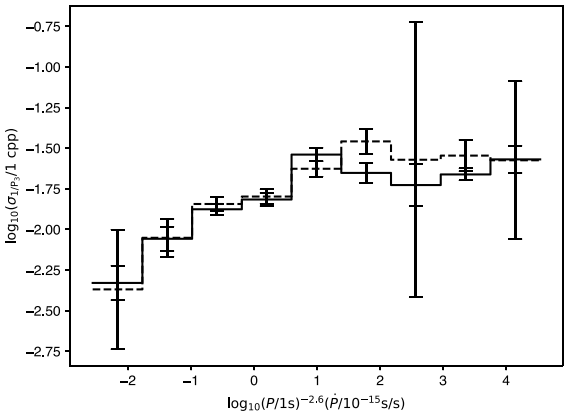

Figure C2. A histogram of the measured (solid) and predicted (dashed) weighted mean $\log_{10}(\sigma_{1/P_3})$ as a function of the combination in P and $\dot{P}$ corresponding to the direction of the strongest correlation in the P–$\dot{P}$ diagram. The prediction is based on equation (5) fitted to the measured distribution. The error bars represent the standard deviation of values contributing to each bin, divided by the square root of the number of values.

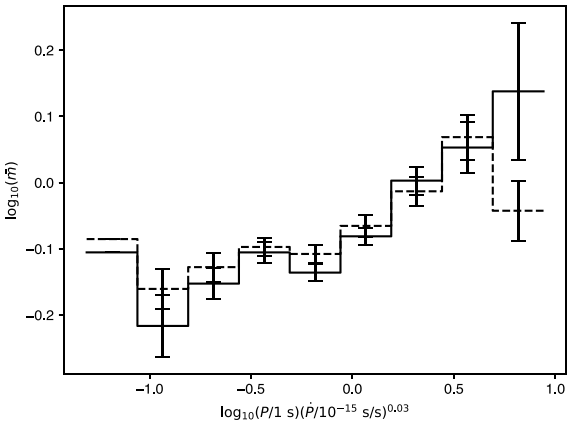

Figure C3. A histogram of the measured (solid) and predicted (dashed) weighted mean $\log_{10}(\bar{m})$ as a function of the combination in P and $\dot{P}$ corresponding to the direction of the strongest correlation in the P–$\dot{P}$ diagram. The prediction is based on equation (5) fitted to the measured distribution. The error bars represent the standard deviation of values contributing to each bin, divided by the square root of the number of values.

with drifting subpulses), the distributions of the two classes of P_3 values are very different, with no evidence for a V-shaped evolution in Fig. C1.

As demonstrated in Section 5.2, the spectral width varies across the P–$\dot{P}$ diagram. Fig. C2 shows that the spectral width shows a significant flattening towards high-$\dot{E}$ pulsars.

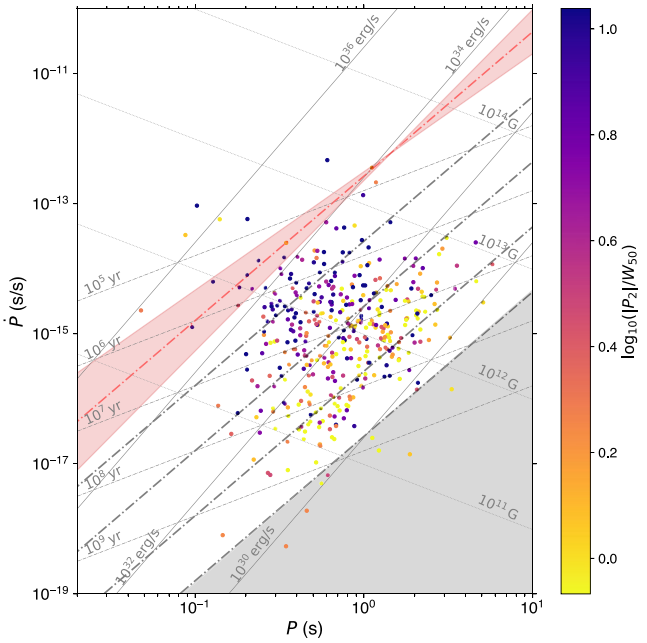

Figure C4. P–$\dot{P}$ diagram where the colours of the dots represent $|P_2|/W_{50}$ for each pulsar with a dominant drifting subpulse feature identified. The dot–dashed lines correspond to constant $|P_2|/W_{50}$ values according to a fit of equation (5) (with $b = 1$ and $c = 0$). The top shaded region indicates the 1σ uncertainty on the slope. See the caption of Fig. 3 for further details.

As shown in Fig. C3, the average modulation index $\bar{m}$ evolution is non-linear in the P–$\dot{P}$ diagram, such that there is flattening of $\bar{m}$ for small-P pulsars. This illustrates why a quadratic form was preferred when performing the fit in Section 5.6. The predicted distributions in Figs C2 and C3 are derived as for Fig. 4.

Fig. C4 shows the distribution of $|P_2|/W_{50}$ for those pulsars with detected drifting subpulses. Large $|P_2|/W_{50}$ are found for higher $\dot{E}$ pulsars, and the values decrease towards lower $\dot{E}$ pulsars. A linear fit of equation (5) (with $c = 0$ and $b = 1$) reveals that the correlation is strong (0.49 ± 0.04) with $a/b = -2.2 \pm 0.4$. The direction of evolution of $|P_2|/W_{50}$ is consistent with both $\dot{E}$ ($a/b = -3$) and τ_c direction ($a/b = -1$).

This paper has been typeset from a TEX/LATEX file prepared by the author.